

Review

# Review of Single Crystal Synthesis of 11 Iron-Based Superconductors

Qiang Hou <sup>†</sup>, Longfei Sun <sup>†</sup>, Yue Sun <sup>\*</sup> and Zhixiang Shi <sup>\*</sup>

School of Physics, Southeast University, Nanjing 211189, China; 230208711@seu.edu.cn (Q.H.); 220222225@seu.edu.cn (L.S.)

\* Correspondence: sunyue@seu.edu.cn (Y.S.); zxshi@seu.edu.cn (Z.S.)

<sup>†</sup> These authors contributed equally to this work.

**Abstract:** The 11 system in the iron-based superconducting family has become one of the most extensively studied materials in the research of high-temperature superconductivity, due to their simple structure and rich physical properties. Many exotic properties, such as multiband electronic structure, electronic nematicity, topology and antiferromagnetic order, provide strong support for the theory of high-temperature superconductivity, and have been at the forefront of condensed matter physics in the past decade. One noteworthy aspect is that a high upper critical magnetic field, large critical current density and lower toxicity give the 11 system good application prospects. However, the research on 11 iron-based superconductors faces numerous obstacles, mainly stemming from the challenges associated with producing high-quality single crystals. Since the discovery of FeSe superconductivity in 2008, researchers have made significant progress in crystal growth, overcoming the hurdles that initially impeded their studies. Consequently, they have successfully established the complete phase diagrams of 11 iron-based superconductors, including  $\text{FeSe}_{1-x}\text{Te}_x$ ,  $\text{FeSe}_{1-x}\text{S}_x$  and  $\text{FeTe}_{1-x}\text{S}_x$ . In this paper, we aim to provide a comprehensive summary of the preparation methods employed for 11 iron-based single crystals over the past decade. Specifically, we will focus on hydrothermal, chemical vapor transport (CVT), self-flux and annealing methods. Additionally, we will discuss the quality, size, and superconductivity properties exhibited by single crystals obtained through different preparation methods. By exploring these aspects, we can gain a better understanding of the advantages and limitations associated with each technique. High-quality single crystals serve as invaluable tools for advancing both the theoretical understanding and practical utilization of high-temperature superconductivity.



**Citation:** Hou, Q.; Sun, L.; Sun, Y.; Shi, Z. Review of Single Crystal Synthesis of 11 Iron-Based Superconductors. *Materials* **2023**, *16*, 4895. <https://doi.org/10.3390/ma16144895>

Academic Editors: Angela Nigro and Paola Romano

Received: 30 May 2023

Revised: 27 June 2023

Accepted: 5 July 2023

Published: 8 July 2023



**Copyright:** © 2023 by the authors. Licensee MDPI, Basel, Switzerland. This article is an open access article distributed under the terms and conditions of the Creative Commons Attribution (CC BY) license (<https://creativecommons.org/licenses/by/4.0/>).

## 1. Introduction

The discovery of iron-based superconductivity represents a significant breakthrough in the field of condensed matter physics, with a profound impact on the study of high-temperature superconductivity [1,2]. According to the different types and ratios of elements in the parent compositions, it can be divided into several different types, such as 111, 122 and 1111 of the iron-pnictide superconductors and 11 and 122 of the iron-chalcogenide superconductors. These materials exhibit a wide range of fascinating physical phenomena, including a multi-band structure, an extremely small Fermi energy, and the presence of nematic and antiferromagnetic (AFM) ordered states. These unconventional superconducting properties make them prime candidates for exploring high-temperature superconductivity and its related properties [3–5]. Importantly, the unconventional superconductivity observed in iron-based materials cannot be explained by the conventional electron–phonon pairing mechanism. This breakthrough challenges the notion that cuprates are the sole class of high-temperature superconductors, thereby stimulating further research into the pairing mechanisms underlying high-temperature superconductivity [6–8].

Compared with FeAs-based superconductors, the 11 iron-based superconductors in iron-chalcogenide compounds have the advantages of a simple crystal structure and non-toxicity. FeSe consists solely of edge-sharing tetrahedral  $\text{FeSe}_4$  layers stacked along the  $c$ -axis, without a charge storage layer [9–11]. A structural transition from tetragonal to orthorhombic occurs at about  $T_s \sim 90$  K accompanied by the nematic phase [12–15]. Despite having a relatively low superconducting critical temperature ( $T_c$ ) of approximately 9 K, high tunability and nematicity without magnetic order have garnered significant attention and research interest. Under high pressure, the  $T_c$  of FeSe can be elevated to approximately 38 K, and a new magnetic order emerges within a specific pressure range once the nematic phase is suppressed [16–19]. Chemical methods, such as intercalation [20,21], ionic liquid gating [22–24] and potassium deposition [25,26], have been employed to raise the  $T_c$  to over 40 K. Remarkably, monolayer FeSe films on doped  $\text{SrTiO}_3$  substrates have exhibited superconductivity with the  $T_c$  surpassing 65 K [27,28]. These materials offer various pathways to achieve a high  $T_c$  and exhibit unconventional superconducting behavior. Consequently, they have become pivotal in advancing research in the field of high-temperature superconductivity, playing a vital role similar to that of copper-based superconductors.

The substitution of isovalent sulfur (S) in FeSe, equivalent to applying positive chemical pressure, has proven to be an effective method for tuning superconductivity and nematic order. With S doping, the nematic transition temperature  $T_s$  gradually decreases until it vanishes at  $x \sim 0.17$ , marking a nonmagnetic nematic quantum critical point (QCP) [29–32]. Nuclear magnetic resonance (NMR) measurements indicate a strong suppression of AFM fluctuations with S substitution, resulting in negligible AFM fluctuations near the QCP [31]. Within the nematic regions, the  $T_c$  exhibits a small superconducting dome, reaching a maximum of 11 K at  $x \sim 0.11$ . Beyond the nematic regions, superconductivity is gradually suppressed, reaching a minimum at  $x \sim 0.45$ , after which the  $T_c$  slowly increases until  $x = 1$  [33]. Notably, unlike when external pressure is applied, no new magnetic order emerges after the nematic phase [33–35].

Similarly, the substitution of isovalent tellurium (Te) in FeSe, equivalent to applying negative chemical pressure, is an effective method for tuning the superconductivity and various ordered states. In  $\text{FeSe}_{1-x}\text{Te}_x$  single crystals phase diagram,  $T_s$  linearly decreases until it disappears at  $x = 0.5$  with Te doping [36–38]. The  $T_c$  initially decreases to a minimum at  $x \sim 0.3$  and then increases to a maximum at  $x \sim 0.6$ ; subsequently, the  $T_c$  is gradually suppressed and antiferromagnetic behavior emerges when  $x > 0.9$  [36,37,39–42]. FeTe undergoes a tetragonal-to-monoclinic structural transition at around 70 K, exhibiting AFM behavior without superconductivity, reminiscent of the emergence of superconductivity from AFM in the cuprate superconductors [43–47]. The unique phase diagram of 11 iron-based superconductors, with its interplay of competing orders, nematic phase, magnetic order and superconductivity, provides important insights for exploring the mechanism of high-temperature superconductivity.

Unfortunately, preparing high-quality single crystals is one of the challenges in the study of the 11 iron-based superconducting system, particularly  $\text{FeSe}_{1-x}\text{Te}_x$  and  $\text{FeSe}_{1-x}\text{S}_x$ . This difficulty is also commonly encountered in the study of other iron-based superconducting families. On the one hand, the low chemical stability of  $\text{FeSe}_{1-x}\text{S}_x$  and the issue of phase separation in  $\text{FeSe}_{1-x}\text{Te}_x$  ( $0 < x < 0.5$ ) make it arduous to obtain single crystals or single-phase samples using traditional solid-state reactions [48–52]. On the other hand, even though the preparation of single crystals of  $\text{FeSe}_{1-x}\text{Te}_x$  ( $0.5 \leq x \leq 1$ ) is relatively straightforward using the self-flux method, the presence of excess Fe significantly affects the investigation of their intrinsic properties, such as the localization of charge carriers [53–55], spin glass phase [56] and incoherent electronic states [54,57]. It is difficult to prepare high-quality single crystals of the 11 system using traditional solid-state reaction methods, and new methods are gradually developed.

To synthesize high quality single crystals across the entire doping range, different methods need to be employed. In this review, we provide an overview of the common synthesis methods for the 11 iron-based system, focusing on the optimal method for

different doping regions, along with a relevant phase diagram of the entire region. Initially, we discuss the conventional methods of obtaining FeSe single crystals, namely the flux method and chemical vapor transport (CVD). In Section 3, we describe the preparation of  $\text{FeSe}_{1-x}\text{S}_x$  single crystals using CVD for range  $0 \leq x \leq 0.29$  and the hydrothermal method for the entire region. In Section 4, we explain how high quality  $\text{FeSe}_{1-x}\text{Te}_x$  ( $0 \leq x \leq 0.5$ ) single crystals can be directly synthesized via CVD. For the Te-high doping region ( $0.5 < x \leq 1$ ), it becomes necessary to anneal the as-grown single crystals in  $\text{O}_2$  or Te vapor. Finally, we conclude the review with a summary and outlook in Section 6.

## 2. Single Crystal Growth and Superconductivity of FeSe

FeSe stands out as one of the most extensively studied materials within the realm of iron-based superconductors, owing to its array of unique properties. Notably, FeSe exhibits a multiband electronic structure, a nematic phase, a BCS-BEC crossover, and spin-density wave (SDW) behavior, all of which benefit from the use of high-quality single crystals. FeSe is considered a multiband compensated semimetal with a Fermi surface consisting of  $d_{xy}$ ,  $d_{yz}$ , and  $d_{xz}$  orbitals, forming well-separated electron and hole pockets [58]. Because the extremely small Fermi energy is comparable to the superconducting energy gap, the superconductivity in FeSe is believed to be situated near the BCS-BEC crossover [59]. Another advantage of FeSe is its non-magnetic properties under normal pressure, making it an ideal platform for investigating the nematic phase and superconductivity [60]. Additionally, SDW in high-quality FeSe single crystals under high-pressure was revealed for the first time [17], which was not observed in previous studies using impure phase samples [16]. Numerous studies have demonstrated that probing the intrinsic properties of FeSe heavily relies on the quality of the single crystals. Consequently, conducting a comprehensive review of FeSe single crystal growth is not only valuable in summarizing existing knowledge, but also offers significant guidance for future FeSe research endeavors.

### 2.1. Flux Method for Growing FeSe Single Crystals

Maw-Kuen Wu's group reported the observation of superconductivity with zero-resistance transition temperature at 8 K in the FeSe polycrystalline bulk for the first time [9]. The crystal of FeSe is composed of a stack of edge-sharing  $\text{FeSe}_4$ -tetrahedra layer-by-layer, as shown schematically in Figure 1. An FeSe single crystal with a size about 500  $\mu\text{m}$  was firstly synthesized using the flux method employing a NaCl/KCl mixed eutectic [61]. The preparation process can be divided into two stages. Firstly,  $\text{Fe}_{1.2}\text{Se}$  polycrystalline with nominal stoichiometry was prepared through a traditional solid-state reaction using high purity Fe and Se powders as the raw materials. Then, the obtained  $\text{Fe}_{1.2}\text{Se}$  polycrystal powder and NaCl/KCl mixed eutectic with mole ratio 1:1 were ground and sealed in an evacuated quartz tube. The quartz tube was slowly heated to 850 °C and kept two hours for sufficient solution of the raw materials and flux. Afterward, the temperature was gradually reduced at a rate of 3 °C/h down to 600 °C, followed by furnace cooling. FeSe single crystals were separated from the flux by dissolving the NaCl/KCl mixed eutectic in deionized water.

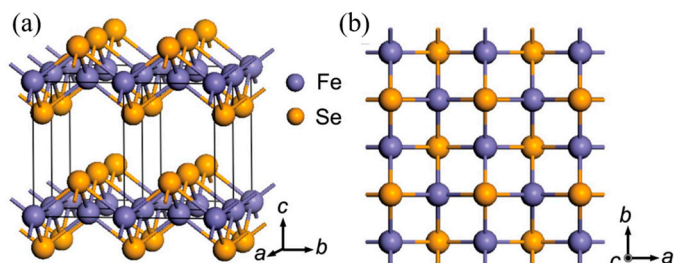


**Figure 1.** Crystal structure of tetragonal FeSe. (a) Perspective view along the  $a$  axis. (b) Parallel view along the  $c$  axis. Reprinted with permission from Ref. [9]. Copyright 2008, copyright the National Academy of Sciences of the USA.

Figure 2 illustrates the basic physical properties of the obtained single crystals. In Figure 2a, the optical image of FeSe reveals two different shapes present in all the grown single crystals: rectangular and hexagonal, both with a size of approximately 500  $\mu\text{m}$ . The X-ray diffraction (XRD) pattern in Figure 2b shows two sets of peaks corresponding to two distinct crystal structures: tetragonal (with space groups P4/nmm) and hexagonal (with space groups P6<sub>3</sub>/mmc). This indicates the presence of non-superconducting impurities in the single crystals. The temperature dependence of resistance and magnetic susceptibility is presented in Figure 2c,d, respectively. The large superconducting transition width ( $\Delta T_c$ ) and the small superconducting volume fraction observed suggest a low-quality superconducting tetragonal phase.

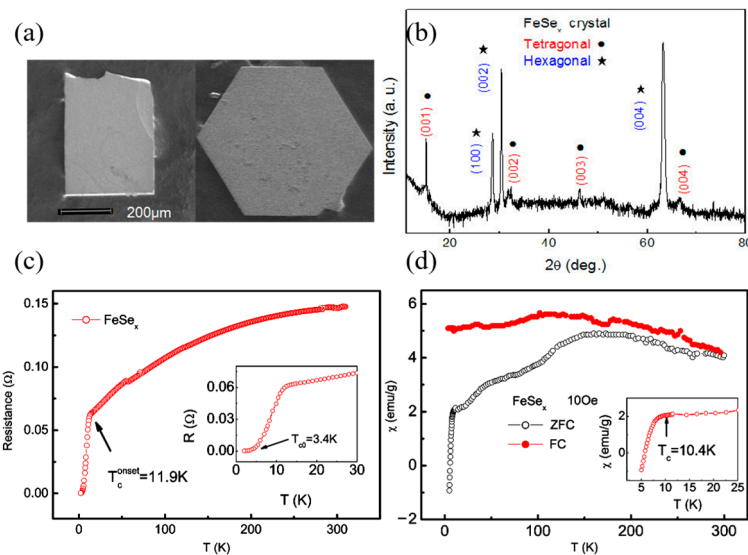


**Figure 2.** (a) Optical image of FeSe with two different shapes, rectangular and hexagonal; (b) XRD pattern from FeSe flake along  $c$  axis, including two sets of peaks; (c) Temperature dependence of resistance for FeSe single crystal in the  $ab$  plane, the inset is a magnified plot in the low temperature region; (d) Temperature dependence of magnetic susceptibility for FeSe single crystal at 10 Oe, the inset is a magnified plot in the low temperature region. Reprinted with permission from Ref. [61]. Copyright 2008, copyright IOP Publishing Ltd.

Subsequently, several research groups successfully synthesized FeSe single crystals using similar methods [62–66]. While superconductivity has improved, the presence of impurities remains a significant concern. Impurities such as hexagonal FeSe, Fe<sub>7</sub>Se<sub>8</sub> and Fe<sub>3</sub>O<sub>4</sub> exist in all as-grown single crystals, posing a major obstacle in understanding the intrinsic properties of FeSe. The strong magnetism of these impurities often results in a prominent ferromagnetic background in the superconducting magnetization-field ( $M$ - $H$ ) loop [63]. FeSe single crystals with no impurity have been synthesized using the LiCl/CsCl flux method where the ferromagnetic background in  $M$ - $H$  loop is nearly absent below the  $T_c$  [67]. However, even with this method, the superconducting volume fraction remains below 60%, indicating the need for further improvements.

## 2.2. Chemical Vapor Transport (CVT) Method for Growing FeSe Single Crystals

Despite the successful growth of large-sized FeSe single crystals using the flux method, the quality of the crystals and the presence of impurities hindered related research. The iodine vapor transport method did not effectively improve the crystal quality [64]. However, a breakthrough was achieved through the preparation of high-quality FeSe single crystals using the CVT method with a KCl/AlCl<sub>3</sub> transport agent [13,68]. A distinct kink at approximately 90 K was observed in the temperature dependence of resistance  $R(T)$  and was confirmed to be a structural(nematic) transition from the tetragonal to orthorhombic phase [12,68–72]. The temperature dependence of resistance and magnetic susceptibility

confirmed the presence of a superconducting transition around 9.4 K. The superconducting transition width of about 1.5 K and a nearly 100% superconducting volume fraction demonstrated good superconductivity [68].

The synthesis process is as follows: High-purity Fe and Se powders were sealed in an evacuated quartz tube along with KCl and  $\text{AlCl}_3$  powders. The quartz tube was horizontally placed in a tube furnace with a double-temperature zone. The hot part of the tube containing the raw materials was heated to 390 °C while the cold part for single crystal growth was kept at 240 °C. After approximately 30 days of transport growth, a large number of single crystals with tetragonal morphology could be observed in the cold part. Similarly to the flux method, FeSe single crystals need to be separated from the flux by dissolving the KCl/ $\text{AlCl}_3$  mixed eutectic in deionized water. The schematic representation of the typical CVT growth assembly is shown in Figure 3a. The scanning electron microscope image in Figure 3b displays the clear layered structure of a tetragonal FeSe single crystal [68]. The temperature dependence of resistivity ( $\rho$ - $T$ ) and magnetization ( $M$ - $T$ ), shown in Figure 3c and inset, indicate high-quality crystallization and good bulk superconductivity [73].

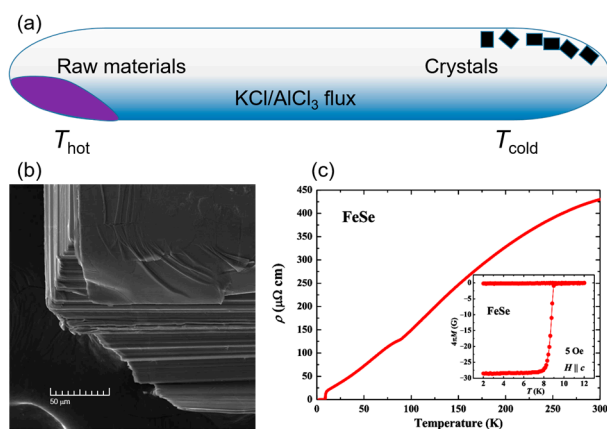


**Figure 3.** (a) Schematic image of the typical CVT growth assembly. (b) The scanning electron microscope image of the layered structure of a tetragonal FeSe single crystal. Reprinted with permission from Ref. [68]. Copyright 2013, copyright the Royal Society of Chemistry. (c) Temperature dependence of resistivity for FeSe single crystal. The inset shows the magnetic susceptibility measured under  $H = 5$  Oe external magnetic field. Reprinted with permission from Ref. [73]. Copyright 2015, copyright the American Physical Society.

Since then, the preparation of FeSe single crystals using similar methods has become more prevalent, leading to a flourishing research landscape, due to the availability of high-quality single crystals. However, the quality of these single crystals is highly sensitive to the preparation conditions, primarily influenced by the complex binary Fe-Se composition–temperature phase diagram [74].

A study conducted by A. E. Böhmer et al. explored the relationship between transition temperatures and residual resistivity ratio (RRR) in vapor-grown FeSe [75]. Their findings revealed that the inclusion of some excess Fe, with an Fe:Se ratio of 1.1:1 as nominal compositions, effectively suppressed the formation of the hexagonal  $\text{Fe}_7\text{Se}_8$  phase. Additionally, the temperature conditions during growth strongly influenced the single crystal quality, with an optimal temperature gradient of 350–390 °C observed in their work. In addition, the tilt angle of the quartz tube can also have some impact on the growth. Figure 4a shows the single crystals under the optimal growth conditions and the schematic picture. Figure 4b,c provides a summary of the correlation between RRR (ratio of resistance at 250 K to resistance just above the  $T_c$ ),  $T_s$  and  $T_c$ . Both the  $T_s$  and  $T_c$  decrease as the RRR increases. Composition analysis using wavelength dispersive X-ray spectroscopy (WDS) indicated no correlation between the  $T_c$  and sample composition. Extrapolating the linear relation

between the  $T_s$  and  $T_c$  suggests that superconductivity would be completely suppressed when the  $T_s$  reaches 64 K.

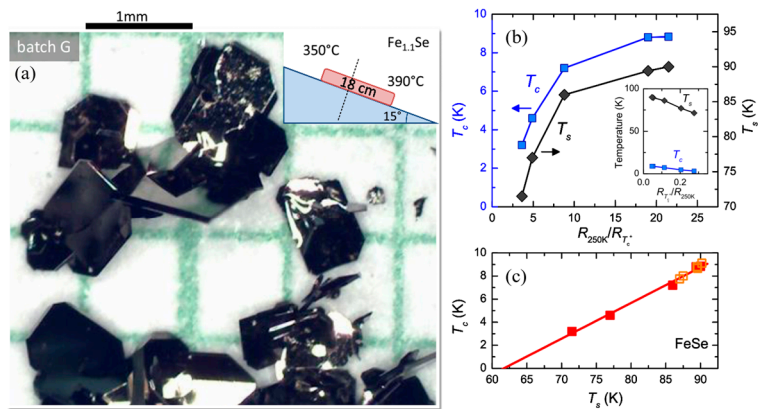


**Figure 4.** (a) Photograph of tetragonal FeSe single crystals under optimal growth conditions and the schematic picture. (b) Structural transition temperature  $T_s$  and superconducting transition temperature  $T_c$  as a function of residual resistivity ratio (ratio of resistance at 250 K to resistance just above  $T_c$ ) for different samples. The inset shows the transition temperature as a function of the inverse residual resistivity ratio. (c)  $T_c$  as a function of  $T_s$  for various samples, Red squares show data from panel (b), and Orange squares represent data on samples grown as part of earlier studies in Ref. [13]. Reprinted with permission from Ref. [75]. Copyright 2016, copyright the American Physical Society.

### 3. Single Crystal Growth and Superconductivity of $\text{FeSe}_{1-x}\text{S}_x$

The nematicity in  $\text{FeSe}_{1-x}\text{S}_x$  is significantly suppressed with S doping, which completely disappears at  $x = 0.17$ . As the S content increases, the nematic fluctuations are strongly enhanced, and the nematic susceptibility diverges as it approaches  $T = 0$ , indicating the presence of a nematic QCP at  $x = 0.17$  [76]. Notably, no AFM fluctuations are observed at the nematic QCP, suggesting a distinct separation between the nematicity and magnetic order. Consequently, the  $\text{FeSe}_{1-x}\text{S}_x$  system proves to be an excellent platform for studying the relationship between the nematicity and superconductivity. Furthermore, the non-Fermi liquid behavior at QCP indicates that nematic critical fluctuations have a significant influence on the normal-state electronic properties [32]. Magnetotransport behavior deviates significantly from the Fermi liquid and linear resistivity at low temperatures within the nematic phase suggest the presence of scattering from low-energy spin fluctuations [31,77,78]. These phenomena provide compelling evidence for the intrinsic connection between quantum criticality, strange metal state, and unconventional superconductivity in the  $\text{FeSe}_{1-x}\text{S}_x$  system.

#### 3.1. CVT Growth of $\text{FeSe}_{1-x}\text{S}_x$ Single Crystals with Low S Doping

$\text{FeSe}_{1-x}\text{S}_x$  single crystals are typically grown by CVT from FeSe up to  $x \sim 0.4$ , using similar preparation methods as FeSe [31,76,77,79,80]. Figure 5a displays the temperature dependence of the resistivity normalized to the value at 300 K value for  $x = 0$  to 0.25. With S doping, a clear kink in resistivity gradually decreases to lower temperatures and disappears at a nonmagnetic nematic QCP,  $x = 0.17$ , as shown more clearly in Figure 5b, depicting the temperature dependence of the first derivative  $d\rho/dT$ . The discovery of QCP with nonmagnetic nematicity in the 11 system has raised the prospect of investigating the role of the relationship between nematicity and superconductivity [32,81].

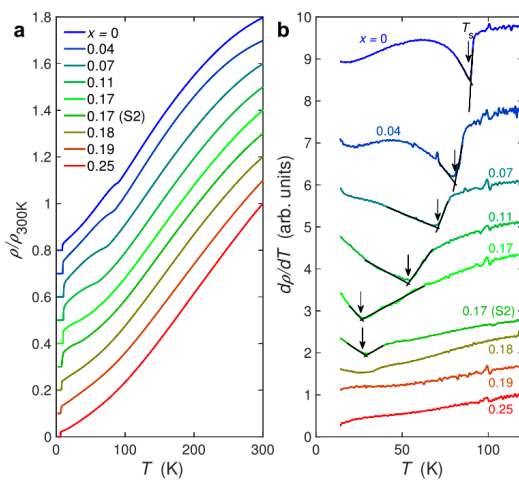


**Figure 5.** Temperature dependence of the resistivity of  $\text{FeSe}_{1-x}\text{S}_x$ . (a) Temperature dependence of resistivity normalized to the 300 K value from  $x = 0$  to 0.25. (b) The first derivative of the resistivity with respect to temperature for the same data. The curves for different S concentrations have been offset for clarity. The location of the structural transition,  $T_s$ , is defined by the intercept of the linear fits on either side of the transition, as indicated by arrows [77].

### 3.2. Hydrothermal Method for Growing $\text{FeSe}_{1-x}\text{S}_x$ Single Crystals across the Entire Doping Range

While the CVT method allows the synthesis of  $\text{FeSe}_{1-x}\text{S}_x$  single crystals with  $x \leq 0.29$ , the hydrothermal method has been employed to overcome this limitation. Xiaofang Lai et al. successfully synthesized tetragonal FeS through the hydrothermal reaction of Fe powder with a sulfide solution and observed bulk superconductivity for the first time at 5 K [34]. Subsequently, a hydrothermal ion release/introduction technique involving the de-intercalation of K ions from  $\text{K}_{0.8}\text{Fe}_{1.6}\text{Se}_{2-x}\text{S}_x$  precursors has been widely utilized for the preparation of FeS and  $\text{FeSe}_{1-x}\text{S}_x$  single crystals [33,82–88], as schematically depicted in Figure 6a. The process involves the growth of  $\text{K}_{0.8}\text{Fe}_{1.6}\text{Se}_{2-x}\text{S}_x$  precursors using the self-flux method, followed by the addition of Fe powder, selenourea, thiourea, and  $\text{K}_{0.8}\text{Fe}_{1.6}\text{Se}_{2-x}\text{S}_x$  single crystals pieces to a solution containing dissolved NaOH in deionized water within a Teflon-linked stainless-steel autoclave (25 mL). The autoclave is then sealed and heated to 130–150 °C for 50–70 h resulting in the formation of  $\text{FeSe}_{1-x}\text{S}_x$  single crystals, as shown in Figure 6b.

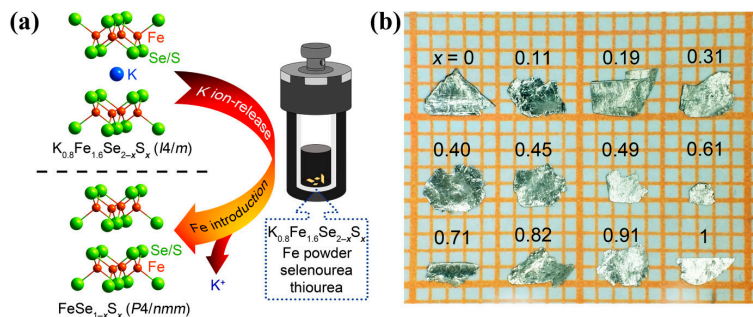


**Figure 6.** (a) Schematic illustration of the hydrothermal ion release/introduction route for the synthesis of  $\text{FeSe}_{1-x}\text{S}_x$  single crystals. (b) Optical image of select  $\text{FeSe}_{1-x}\text{S}_x$  single crystals. Reprinted with permission from Ref. [33]. Copyright 2021, copyright the American Physical Society.

Figure 7 presents a comprehensive phase diagram of  $\text{FeSe}_{1-x}\text{S}_x$  single crystals, encompassing the entire region obtained from the hydrothermal method [33] and a partial region ( $0 \leq x \leq 0.29$ ) obtained from the CVT method [31,76,77]. The values of the  $T_s$  and  $T_c$  obtained from the hydrothermal method are slightly lower than those from the CVT method, possibly due to disorder effects in the crystals [75]. The exponent “ $n$ ” in the contour plot corresponds to the power law,  $\rho(T) = \rho_0 + AT^n$ , where  $\rho_0$  represents the residual

resistivity. In the nematic phase, the resistivity exhibits a non-Fermi liquid behavior characterized by sublinear temperature dependence. Outside the nematic phase, the resistivity at low temperatures follows a perfect Fermi liquid behavior, i.e.,  $T^2$  dependence. In the Fermi liquid region, the coefficient  $A$  decreases monotonically with S doping, indicating a reduction in effective mass, since  $A$  is proportional to the carrier effective mass according to the Landau Fermi liquid theory. Below the characteristic temperature  $T^*$ , the resistivity displays an anomalous upturn just before the superconducting transition. The origin of this anomaly may be attributed to local magnetic impurity scattering or inelastic scattering due to crystallographic disorder.

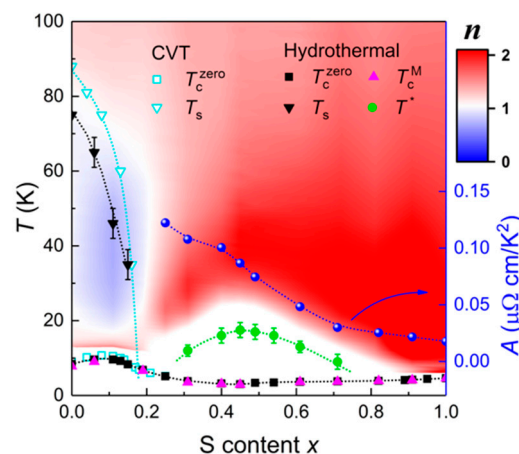


**Figure 7.** Complete phase diagram of  $\text{FeSe}_{1-x}\text{S}_x$  single crystals.  $T_s$  represents the nematic transition temperature.  $T_c^{\text{zero}}$  and  $T_c^M$  are the SC transition temperatures obtained from resistivity and magnetization measurements, respectively.  $T^*$  is the characteristic temperature at which the  $\rho$ - $T$  curves show local minima at low temperatures. Reprinted with permission from Ref. [33]. Copyright 2021, copyright the American Physical Society.

#### 4. Single Crystal Growth and Superconductivity of $\text{FeSe}_{1-x}\text{Te}_x$

Similar to S doping, the nematicity in  $\text{FeSe}_{1-x}\text{Te}_x$  is gradually suppressed with Te doping and disappears at  $x = 0.5$  [36,37]. The presence of nematic QCP accompanied by the superconducting dome is supported by the behavior of the nematic susceptibility in  $\text{FeSe}_{1-x}\text{Te}_x$  single crystals [89]. The magnetic order disappears under high pressure when  $x > 0.1$ , while the superconducting dome persists, suggesting that the enhancement of superconductivity in  $\text{FeSe}_{1-x}\text{Te}_x$  is not attributed to magnetism but rather to the nematic fluctuations [37]. In the case of higher Te content,  $\text{FeSe}_{1-x}\text{Te}_x$  exhibits topological surface superconductivity and the presence of Majorana fermions, making it the first high-temperature topological superconductor to be discovered [90,91]. In the region near  $\text{FeTe}$ , a competition between magnetism and superconductivity is also observed [40,42]. The magnetism in  $\text{FeSe}_{1-x}\text{Te}_x$  exhibits a bi-collinear antiferromagnetism, which is distinct from the collinear antiferromagnetism observed in iron-pnictides [43]. Additionally,  $\text{FeSe}_{1-x}\text{Te}_x$  displays an excellent high upper critical field and low anisotropy, which significantly reduce the challenges associated with applications [92]. Researchers have successfully overcome the effects of excess iron and, more recently, phase separation, and the intrinsic properties of  $\text{FeSe}_{1-x}\text{Te}_x$  are gradually being unveiled.

##### 4.1. CVT Growth of $\text{FeSe}_{1-x}\text{Te}_x$ ( $0 \leq x \leq 0.5$ ) Single Crystals

While high-quality single crystals of  $\text{FeSe}_{1-x}\text{S}_x$  have been successfully obtained, achieving homogenous Te-doping single crystals remains challenging due to strict preparation conditions and the phase separation in the region of  $0.1 \leq x \leq 0.4$  [38,51,52]. In recent years, significant efforts have been made in crystal growth, leading to several studies on phase separation regions. The synthesis of  $\text{FeSe}_{1-x}\text{Te}_x$  ( $0 \leq x \leq 0.41$ ) single crystals using

the flux method with a temperature gradient, including the phase separation regions, has been reported for the first time [36].

Figure 8a illustrates the schematic diagram of the growth setup, where a horizontal quartz tube is placed in a two-temperature zone tube furnace. The mixture of high-purity Fe, Se and Te powders, pre-sintered at 450 °C, along with a flux mixture of AlCl<sub>3</sub>/KCl was placed in high-temperature zone of quartz tube. After 20–30 days, flake-like single crystals were obtained in the low-temperature zone and the residual flux was removed by dissolving it in distilled water, as shown in Figure 8b. Then, a FeSe<sub>0.67</sub>Te<sub>0.33</sub> single crystal was grown using a flux method with a single-temperature zone in a box furnace [38].

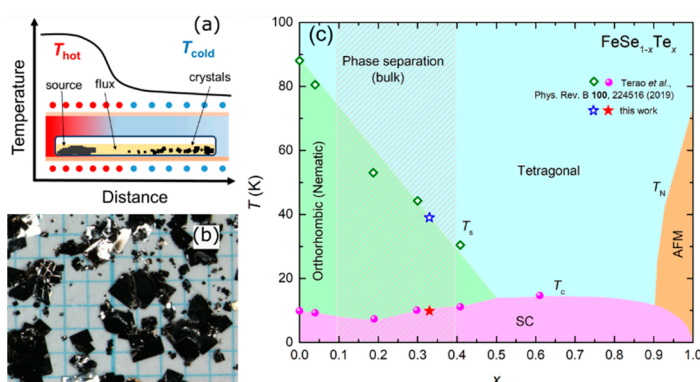


**Figure 8.** (a) Schematic image of the temperature distribution in the horizontal tube furnace for single-crystal growth of FeSe<sub>1-x</sub>Te<sub>x</sub> by the flux method. Reprinted with permission from Ref. [36]. Copyright 2019, copyright the American Physical Society. (b) Photograph of as-grown single crystals of FeSe<sub>1-x</sub>Te<sub>x</sub> after removing the flux. Reprinted with permission from Ref. [36]. Copyright 2019, copyright the American Physical Society. (c) Complete temperature-doping  $x$  phase diagram of FeSe<sub>1-x</sub>Te<sub>x</sub> single crystals. Reprinted with permission from Ref. [38]. Copyright 2021, copyright the IOP Publishing.

The results of these two works are summarized in a phase diagram, shown in Figure 8c. The  $T_c$  exhibits a minimum around  $x \sim 0.2$ , which is attributed to the effect of sample disorder, as indicated by the relatively small RRR value [36,75]. The  $T_s$  decreases linearly with increasing Te doping and disappears at approximately  $x \sim 0.5$ . The  $T_c$  exhibits a maximum around  $x \sim 0.6$ , and the Néel temperature ( $T_N$ ) starts to appear when  $x > 0.9$ , accompanied by the suppression of superconductivity [93]. The breakthrough in the phase separation region provides a promising approach for the preparation of high-quality single crystals, particularly in the phase separation region, enabling the investigation of the evolution of the intrinsic properties of FeSe<sub>1-x</sub>Te<sub>x</sub> with Te doping.

Recently, significant progress has been made in the growth of high-quality FeSe<sub>1-x</sub>Te<sub>x</sub> ( $0 \leq x \leq 0.5$ ) single crystals using the CVT method, and the temperature–composition phase diagrams have been established, as shown in Figure 9 [37]. Similar to the flux method with a two-temperature zone described earlier, the mixture of Fe, Se, and Te powders was sealed in a quartz ampoule with transport agents AlCl<sub>3</sub>/KCl and the growth time was 1–2 weeks. The temperatures of the hot and cold sides were controlled at 420 and 250 °C for  $0 \leq x \leq 0.25$  (620 and 450 °C for  $0.25 \leq x \leq 0.55$ ), respectively, which play a significant role in the crystal growth process.

Despite the similar synthesis methods employed by different research groups, there is considerable variation in the quality of the obtained single crystals, including RRR, the superconducting transition temperature  $T_c$  and transition width  $\Delta T$ . In this systematic study, a comprehensive analysis of RRR with a large number of data points, represented by  $\rho(200 \text{ K})/\rho(15 \text{ K})$ , reveals a monotonous decrease with increasing Te concentration, as shown in Figure 9c. This suggests an intrinsic origin of the minimum  $T_c$  observed at  $x = 0.3$ . Additionally, when considering the temperature–pressure–composition phase diagrams of

$\text{FeSe}_{1-x}\text{Te}_x$  ( $0 \leq x \leq 0.5$ ) single crystals, it is proposed that nematic fluctuations play a role in enhancing the  $T_c$  above  $x = 0.3$  and contribute to the formation of the observed  $T_c$ -dip.

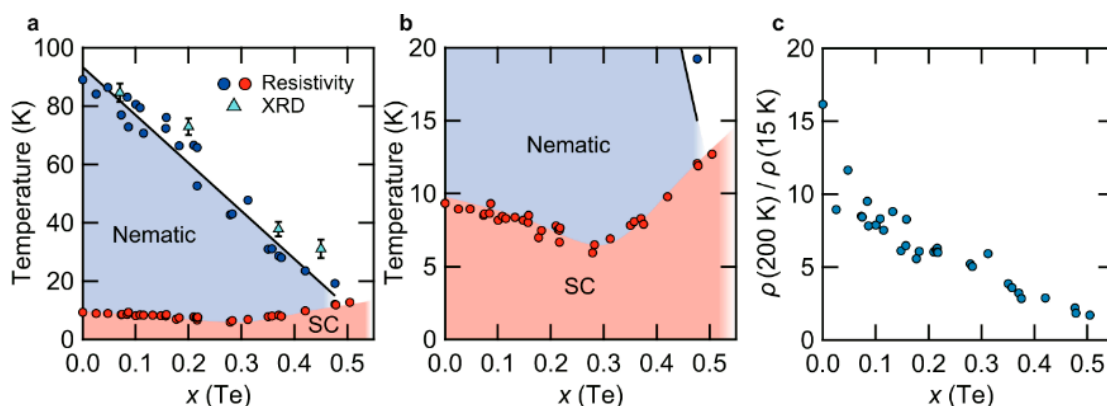


**Figure 9.** (a) Temperature— $x$  (Te) phase diagram of  $\text{FeSe}_{1-x}\text{Te}_x$  ( $0 \leq x \leq 0.5$ ) single crystals. (b) The same as in (a), but the temperature range is 0–20 K. (c) Dependence of  $\rho(200 \text{ K})/\rho(15 \text{ K})$  on  $x$  (Te) extracted from the resistivity data [37].

#### 4.2. Self-Flux Plus Annealing Method for Growing $\text{FeSe}_{1-x}\text{Te}_x$ ( $0.5 < x \leq 1$ ) Single Crystals

$\text{FeSe}_{1-x}\text{Te}_x$  ( $0.5 < x \leq 1$ ) single crystals can be grown using standard melting methods, such as the Bridgeman method [50], self-flux method (a modified Bridgeman method, similar to each other) [94,95] and optical zone melting [96]. In the self-flux method, high-purity Fe, Se and Te powders with nominal ratios were loaded into a quartz tube, which was then evacuated and sealed. To prevent cracking during the growth process, it is necessary to seal the quartz tube into a larger quartz tube. The assembly was slowly heated to 1050 °C and sustained for 24 h, followed by cooling down to 710 °C at a rate of 3 °C/h and furnace cooling. The obtained single crystals have a mirror-like surface and can reach the centimeter scale sizes, as shown in Figure 10a [97].

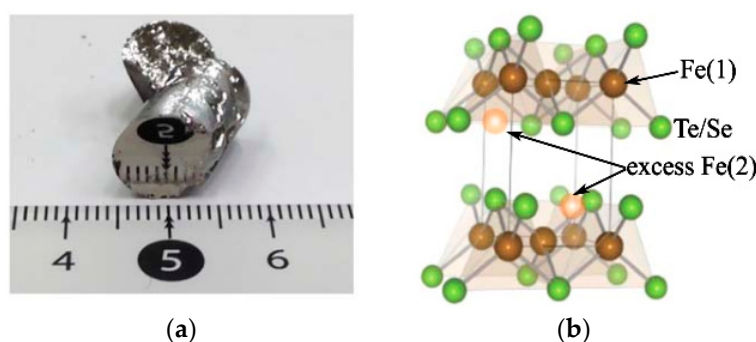


**Figure 10.** (a) Photograph of the as-grown  $\text{FeTe}_{0.6}\text{Se}_{0.4}$  single crystal. Reprinted with permission from Ref. [97]. Copyright 2015, copyright the IOP Publishing, Ltd. (b) Crystal structure of  $\text{FeSe}_{1-x}\text{Te}_x$ . The green ball represents the Fe(1) in tetragonal lattice, and the orange ball represents the excess Fe(2) [98]. Reprinted with permission from Ref. [41]. Copyright 2019, copyright the IOP Publishing, Ltd.

The position of excess iron in the crystal structure is shown in Figure 10b, marked by the orange ball. Excess Fe in the crystal structure of  $\text{FeSe}_{1-x}\text{Te}_x$  significantly affects its intrinsic properties, such as localization of the charge carriers [53–55], spin glass phase [56] and incoherent electronic states [54,57]. Annealing processes have been developed to effectively remove excess Fe.  $\text{FeTe}_{0.61}\text{Se}_{0.39}$  single crystals were successfully annealed in a vacuum environment for the first time at 400 °C for more than 10 days, resulting in a sharp superconducting transition at around 14 K [99]. Subsequently, vacuum annealing techniques have been applied to remove excess Fe from  $\text{FeSe}_{1-x}\text{Te}_x$  ( $0.5 < x \leq 1$ ) single crystals [93,100]. It was reported that  $\text{N}_2$  annealing can also effectively remove excess

Fe [101]. However, it was later discovered that vacuum and  $N_2$  annealing have no effect on the excess Fe, and the observed improvement was actually due to the action of a small amount of residual  $O_2$  present during the annealing process [102]. Apart from  $O_2$  annealing, elements such as Te, Se, S, P, As, I, and Sb have been proven to effectively remove excess Fe through vapor annealing for  $FeSe_{1-x}Te_x$  ( $0.5 < x \leq 1$ ) single crystals [103–108]. For efficiency and nontoxicity, we focus on providing a detailed introduction using  $O_2$  annealing to remove excess Fe.

Figure 11 shows the schematic picture of the annealing system used for  $O_2$  [41]. To perform the  $O_2$  annealing, as-grown single crystals were cut and cleaved into thin slices with dimensions of about  $2.0 \times 1.0 \times 0.05$  mm $^3$ . These slices were then weighed and loaded into a quartz tube with an inner diameter of 10 mm. The quartz tube was carefully evacuated using a diffusion pump, and the pressure in the tube was detected using a diaphragm-type manometer with an accuracy greater than 1 mTorr. Once the gas was fully removed, the quartz tube was filled with Ar/ $O_2$  (1% Ar) mixed gas and sealed to a length of 100 mm. The pressure in the system is continuously monitored during the sealing process to prevent gas leakage and control the  $O_2$  pressure in the quartz tube. The crystals were then annealed at 400 °C for various periods of time and subsequently quenched in water.

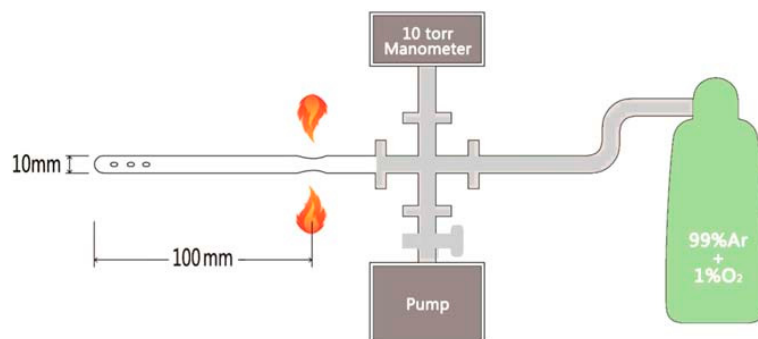


**Figure 11.** Schematic picture of the annealing system for sealing the crystal in quartz tube with a controlled amount of  $O_2$ . Reprinted with permission from Ref. [41]. Copyright 2019, copyright the IOP Publishing, Ltd.

The doping–temperature phase diagram for the as-grown and annealed  $Fe_{1+y}Te_{1-x}Se_x$  ( $0 \leq x \leq 0.43$ ,  $y$  represents excess Fe) were established based on the magnetization, magnetic susceptibility, resistivity, and Hall effects, as shown in Figure 12a,b, respectively [39]. In the as-grown, there is a clear spin glass state originating from excess Fe in the interstitial site before the onset of superconductivity. The superconductivity observed in the as-grown crystals is not of bulk nature and can only be obviously detected through the temperature dependence of resistivity. After annealing, significant changes in superconductivity and magnetic order are observed. The AFM phase is suppressed into a very narrow regions for  $x$  (Se)  $< 0.05$ , and the spin glass state completely disappears. This confirms the effective removal of excess Fe through annealing. The superconducting state exhibits a clear bulk effect and can be easily detected by magnetic measurements.

In our recent work, we have successfully prepared high-quality full-range  $FeSe_{1-x}Te_x$  single crystals, with varying Te doping levels ( $0 \leq x \leq 0.5$  by CVT and  $0.5 < x \leq 1$  by the flux method plus annealing). The corresponding phase diagram is illustrated in Figure 13. Notably, Te doping gradually suppresses the nematic phase until it completely disappears at  $x = 0.5$ . Our results also reveal that the  $T_c$  reaches its minimum at  $x = 0.3$ , which aligns with the findings of Mukasa et al. [37], further supporting the intrinsic nature of the  $T_c$ -dip phenomenon observed in  $FeSe_{1-x}Te_x$ . Subsequently, the  $T_c$  increases and reaches a maximum at  $x = 0.6$  but gradually decreases upon further Te doping, eventually leading to a transition into a non-superconducting antiferromagnetic state.

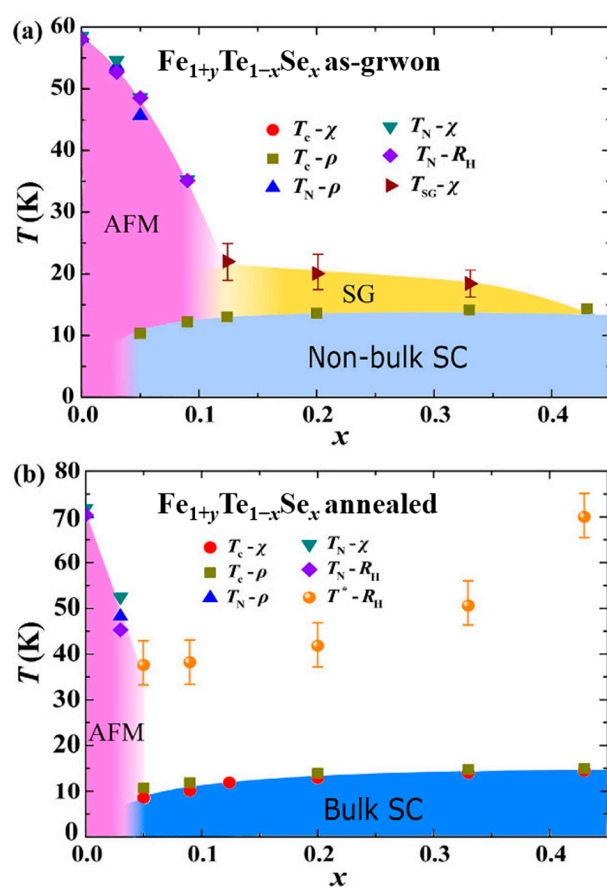


**Figure 12.** The doping–temperature ( $x$ - $T$ ) phase diagrams for  $\text{Fe}_{1+y}\text{Te}_{1-x}\text{Se}_x$  ( $0 \leq x \leq 0.43$ ,  $y$  represents excess Fe) single crystals (a) before and (b) after  $\text{O}_2$  annealing obtained from magnetization, magnetic susceptibility, resistivity and Hall effect measurements [39].

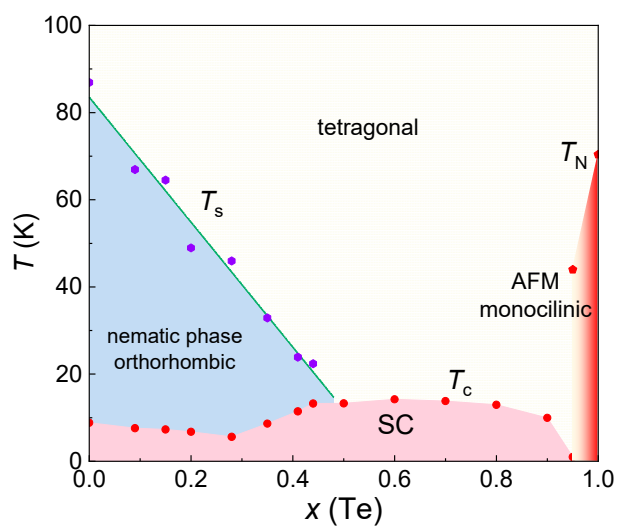


**Figure 13.** Complete phase diagram of  $\text{FeSe}_{1-x}\text{Te}_x$  ( $0 \leq x \leq 1$ ) single crystals in our recent work.

The high chemical stability, high  $T_c$ , and strong upper critical field exhibited by  $\text{FeSe}_{1-x}\text{Te}_x$  single crystals make them excellent candidates for investigating the pairing mechanism underlying high-temperature superconductivity. Consequently, the comprehensive phase diagram we have established for  $\text{FeSe}_{1-x}\text{Te}_x$  provides valuable support for the ongoing exploration of the superconducting pairing mechanism in high-temperature superconductors.

#### 4.3. Optical Zone-Melting Technique for Growing $\text{FeSe}_{1-x}\text{Te}_x$ Single Crystals

$\text{FeSe}_{1-x}\text{Te}_x$  single crystals also can be grown using the optical zone-melting technique [96,109]. This method allows for real-time observation of single crystal growth and precise control of the growth rate by visualizing the melting zone. Figure 14 illustrates the schematic picture of a single crystal growth and shows a large-sized single crystal obtained using this technique. The growth process is as follows:

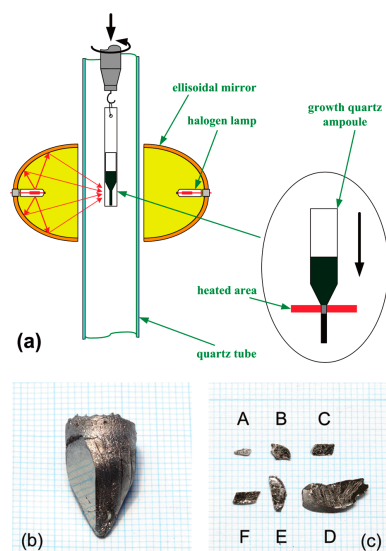


**Figure 14.** (a) Schematic diagram of apparatus setup of the optical zone-melting method. The red arrows represent the light path of the light source, and the black arrow represents the direction of single crystal growth. (b) Single crystal boule of as-grown  $\text{FeTe}_{0.7}\text{Se}_{0.3}$  single crystal on a 1 mm grid. The shiny surface is the a-b plane. (c) The crystal flakes with the (001) face. Crystals from A–F represent  $\text{FeSe}_x\text{Te}_{1-x}$  single crystals of  $x = 0.3, 0.5, 0.6, 0.7, 0.9$ , and 1.0, respectively. Reprinted with permission from Ref. [96]. Copyright 2009, copyright the American Chemical Society.

High-purity powders of Fe, Se and Te with a nominal ratio were mixed in a ball mill for 4 h. The mixed powders were cold pressed into discs under a uniaxial pressure of  $400 \text{ kg}\cdot\text{cm}^{-2}$ , and then heated at  $600^\circ\text{C}$  for 20 h under a vacuum. The reacted bulk material was reground into a fine powder and loaded into a double quartz tube. The tube was loaded in an optical zone-melting furnace equipped with two 1500 W halogen lamps as infrared radiation sources, as shown in Figure 14. The tube was rotated at a rate of 20 rpm and moved at a rate of  $1\text{--}2 \text{ mm}\cdot\text{h}^{-1}$ . After the growth, the as-grown crystals undergo an annealing process: ramping to  $700\text{--}800^\circ\text{C}$  in 7 h, holding for 48 h; cool to  $420^\circ\text{C}$  in 4 h, hold for 30 h; and finally shutting down the furnace and cooling to room temperature.

Despite obtaining large-sized and well-crystallized single crystals using the optical zone-melting technique, the upwarping behavior of the  $R(T)$  curves before superconducting transition is still apparent, indicating the presence of excess Fe in the crystals [96]. Moreover, due to the complexity of the preparation process and the more established self-flux method, the optical zone-melting method is not commonly used for the growth of  $\text{FeSe}_{1-x}\text{Te}_x$  single crystals.

#### 5. Single Crystal Growth and Superconductivity of $\text{FeTe}_{1-x}\text{S}_x$

$\text{FeTe}_{1-x}\text{S}_x$  system also exhibits superconductivity. Yoshikazu Mizuguchi et al. first reported the superconductivity in the  $\text{FeTe}_{1-x}\text{S}_x$  system and found that the  $T_c$  can reach 10 K when  $x$  is 0.2 [110].  $\text{FeTe}_{1-x}\text{S}_x$  single crystals with low S doping were grown using the self-flux method, similar to  $\text{FeSe}_{1-x}\text{Te}_x$  ( $0.5 < x \leq 1$ ) single crystals [111–115]. Annealing treatment is also necessary to improve superconductivity for  $\text{FeTe}_{1-x}\text{S}_x$  single crystals, although the excess Fe cannot be completely removed [116–121]. The solubility limit of

S in FeTe is about 12% and Chiheng Dong et al. provided the phase diagram in this region [119,122]. With S doping, AFM is suppressed and superconductivity is enhanced.

Caiye Zhao et al. successfully synthesized a series of  $\text{FeS}_{1-x}\text{Te}_x$  ( $0 \leq x \leq 0.15$ ) single crystals by a hydrothermal method for the first time and provided a phase diagram of  $\text{FeS}_{1-x}\text{Te}_x$  single crystals, shown in Figure 15 [123]. The  $T_c$  is rapidly suppressed with the Te doping for  $\text{FeS}_{1-x}\text{Te}_x$  ( $0 \leq x \leq 0.15$ ) single crystals and finally disappears when  $x > 0.1$ . Due to the large solution limited region, only a small amount of doping can be applied at both ends of the phase diagram. The complete phase diagram needs further exploration.

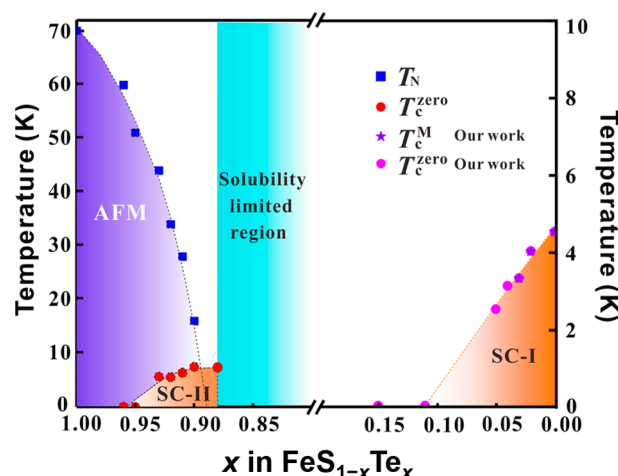


**Figure 15.** The doping phase diagram of  $\text{FeS}_{1-x}\text{Te}_x$  single crystals [119,123].

## 6. Conclusions

In conclusion, significant progress has been made in the preparation of 11 system single crystals, including  $\text{FeSe}_{1-x}\text{Te}_x$  and  $\text{FeSe}_{1-x}\text{S}_x$ , through various methods. A comprehensive phase diagram has been constructed, as depicted in Figure 16, summarizing the superconducting transition temperatures ( $T_c$ ), the onset of nematic phase ( $T_s$ ), and the Néel temperature ( $T_N$ ) for the single crystals prepared using the optimal techniques in different intervals.

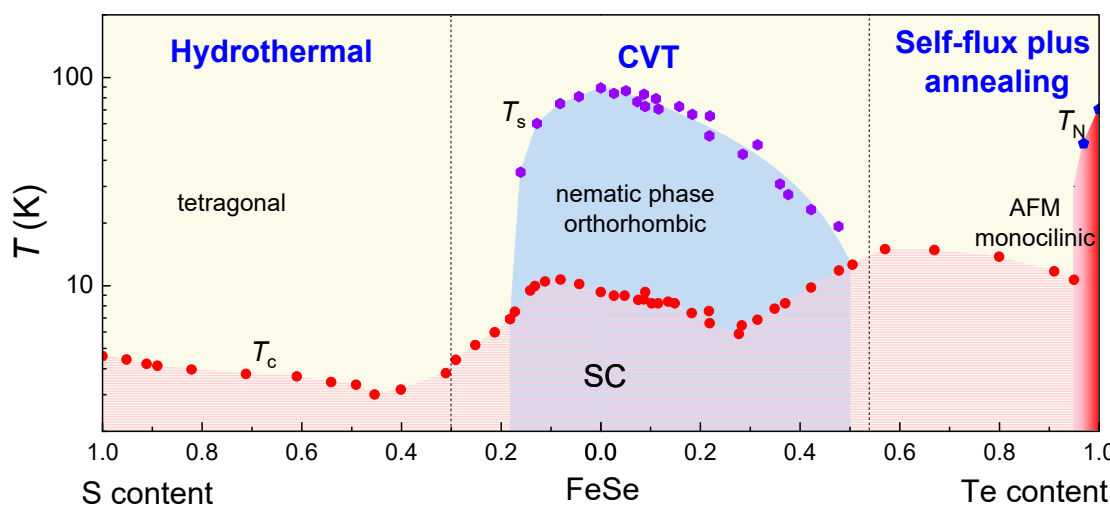


**Figure 16.** The entire phase diagram of  $\text{FeSe}_{1-x}\text{Te}_x$  and  $\text{FeSe}_{1-x}\text{S}_x$  single crystals synthesized by the optimal methods, hydrothermal for  $\text{FeSe}_{1-x}\text{S}_x$  ( $0.29 \leq x \leq 1$ ) [33], CVT for  $\text{FeSe}_{1-x}\text{S}_x$  ( $0 \leq x \leq 0.29$ ) [31,76,77] and  $\text{FeSe}_{1-x}\text{Te}_x$  ( $0 \leq x \leq 0.55$ ) [37] and self-flux plus annealing for  $\text{FeSe}_{1-x}\text{Te}_x$  ( $0.55 \leq x \leq 1$ ) [39].

High quality  $\text{FeSe}_{1-x}\text{S}_x$  ( $0 \leq x \leq 0.29$ ) and  $\text{FeSe}_{1-x}\text{Te}_x$  ( $0 \leq x \leq 0.55$ ) single crystals are typically grown using CVT method with  $\text{AlCl}_3/\text{KCl}$  transport agent. It is fortuitous that the range encompassing these single crystals includes the nematic phase without magnetic order. The exceptional quality of these crystals serves as an excellent platform for investigating the interplay between nematicity and superconductivity.  $\text{FeSe}_{1-x}\text{S}_x$  ( $0.29 \leq x \leq 1$ ) single crystals, however, can only be synthesized using hydrothermal method. Although the quality of single crystals using hydrothermal is slightly inferior to those grown using CVT, they still hold great significance for studying the complete phase diagram of  $\text{FeSe}_{1-x}\text{S}_x$ . By utilizing the self-flux plus annealing technique, single crystals without excess Fe in the highly Te doping region can be obtained. In this particular region, the  $T_c$  reaches maximum of the entire phase diagram, approximately 15 K, occurring around  $x(\text{Te}) \sim 0.6$ . Furthermore, AFM state is observed within a narrow region around  $\text{FeTe}$ .

The connection between the ordered states and superconductivity have not been well resolved, and the relationship between nematicity and SDW has been described as a “chicken-egg” problem [10]. Understanding the interplay between these states is complex and challenging. Furthermore, the behavior of superconductivity throughout the entire phase diagram presents intricate twists and turns, adding to the puzzle. In summary, the establishments of the comprehensive phase diagram for the 11 iron-based system is of utmost importance for unraveling the mechanism behind high-temperature superconductivity and for discovering novel superconducting materials.

**Author Contributions:** Q.H. and L.S. designed and wrote the manuscript with the help of Y.S. and Z.S. All authors have read and agreed to the published version of the manuscript.

**Funding:** This research was funded by the National Key R&D Program of China (Grant No. 2018YFA0704300), the Strategic Priority Research Program (B) of the Chinese Academy of Sciences (Grant No. XDB25000000).

**Institutional Review Board Statement:** Not applicable.

**Informed Consent Statement:** Not applicable.

**Data Availability Statement:** The data used to support the findings of this study are available upon request from the corresponding author.

**Conflicts of Interest:** The authors declare no conflict of interest.

## References

1. Kamihara, Y.; Hiramatsu, H.; Hirano, M.; Kawamura, R.; Yanagi, H.; Kamiya, T.; Hosono, H. Iron-Based Layered Superconductor: LaOFep. *J. Am. Chem. Soc.* **2006**, *128*, 10012–10013. [[CrossRef](#)]
2. Kamihara, Y.; Watanabe, T.; Hirano, M.; Hosono, H. Iron-Based Layered Superconductor  $\text{La}[\text{O}_{1-x}\text{F}_x]\text{FeAs}$  ( $x = 0.05 – 0.12$ ) with  $T_c = 26$  K. *J. Am. Chem. Soc.* **2008**, *130*, 3296–3297. [[CrossRef](#)] [[PubMed](#)]
3. Wen, H.-H.; Li, S. Materials and Novel Superconductivity in Iron Pnictide Superconductors. *Annu. Rev. Condens. Matter Phys.* **2011**, *2*, 121–140. [[CrossRef](#)]
4. Thewalt, E.; Hayes, I.M.; Hinton, J.P.; Little, A.; Patankar, S.; Wu, L.; Helm, T.; Stan, C.V.; Tamura, N.; Analytis, J.G.; et al. Imaging Anomalous Nematic Order and Strain in Optimally Doped  $\text{BaFe}_2(\text{As},\text{P})_2$ . *Phys. Rev. Lett.* **2018**, *121*, 027001. [[CrossRef](#)]
5. Shibauchi, T.; Carrington, A.; Matsuda, Y. A Quantum Critical Point Lying Beneath the Superconducting Dome in Iron Pnictides. *Annu. Rev. Condens. Matter Phys.* **2014**, *5*, 113–135. [[CrossRef](#)]
6. Mazin, I.I. Superconductivity Gets an Iron Boost. *Nature* **2010**, *464*, 183–186. [[CrossRef](#)] [[PubMed](#)]
7. Hirschfeld, P.J.; Korshunov, M.M.; Mazin, I.I. Gap Symmetry and Structure of Fe-Based Superconductors. *Rep. Prog. Phys.* **2011**, *74*, 124508. [[CrossRef](#)]
8. Chubukov, A. Pairing Mechanism in Fe-Based Superconductors. *Annu. Rev. Condens. Matter Phys.* **2012**, *3*, 57–92. [[CrossRef](#)]
9. Hsu, F.-C.; Luo, J.-Y.; Yeh, K.-W.; Chen, T.-K.; Huang, T.-W.; Wu, P.M.; Lee, Y.-C.; Huang, Y.-L.; Chu, Y.-Y.; Yan, D.-C.; et al. Superconductivity in the PbO-Type Structure  $\alpha$ -FeSe. *Proc. Natl. Acad. Sci. USA* **2008**, *105*, 14262–14264. [[CrossRef](#)]
10. Shibauchi, T.; Hanaguri, T.; Matsuda, Y. Exotic Superconducting States in FeSe-Based Materials. *J. Phys. Soc. Jpn.* **2020**, *89*, 102002. [[CrossRef](#)]
11. Chen, T.-K.; Chang, C.-C.; Chang, H.-H.; Fang, A.-H.; Wang, C.-H.; Chao, W.-H.; Tseng, C.-M.; Lee, Y.-C.; Wu, Y.-R.; Wen, M.-H.; et al. Fe-Vacancy Order and Superconductivity in Tetragonal  $\beta$ - $\text{Fe}_{1-x}\text{Se}$ . *Proc. Natl. Acad. Sci. USA* **2014**, *111*, 63–68. [[CrossRef](#)]

12. McQueen, T.M.; Williams, A.J.; Stephens, P.W.; Tao, J.; Zhu, Y.; Ksenofontov, V.; Casper, F.; Felser, C.; Cava, R.J. Tetragonal-to-Orthorhombic Structural Phase Transition at 90 K in the Superconductor  $\text{Fe}_{1.01}\text{Se}$ . *Phys. Rev. Lett.* **2009**, *103*, 057002. [CrossRef] [PubMed]
13. Böhmer, A.E.; Hardy, F.; Eilers, F.; Ernst, D.; Adelmann, P.; Schweiss, P.; Wolf, T.; Meingast, C. Lack of Coupling between Superconductivity and Orthorhombic Distortion in Stoichiometric Single-Crystalline FeSe. *Phys. Rev. B* **2013**, *87*, 180505. [CrossRef]
14. Fernandes, R.M.; Chubukov, A.V.; Schmalian, J. What Drives Nematic Order in Iron-Based Superconductors? *Nat. Phys.* **2014**, *10*, 97–104. [CrossRef]
15. Rößler, S.; Coduri, M.; Tsirlin, A.A.; Ritter, C.; Cuello, G.; Koz, C.; Muzica, L.; Schwarz, U.; Rößler, U.K.; Wirth, S.; et al. Nematic State of the FeSe Superconductor. *Phys. Rev. B* **2022**, *105*, 064505. [CrossRef]
16. Medvedev, S.; McQueen, T.M.; Troyan, I.A.; Palasyuk, T.; Eremets, M.I.; Cava, R.J.; Naghavi, S.; Casper, F.; Ksenofontov, V.; Wortmann, G.; et al. Electronic and Magnetic Phase Diagram of  $\beta\text{-Fe}_{1.01}\text{Se}$  with Superconductivity at 36.7 K under Pressure. *Nat. Mater.* **2009**, *8*, 630–633. [CrossRef]
17. Sun, J.P.; Matsuura, K.; Ye, G.Z.; Mizukami, Y.; Shimozawa, M.; Matsubayashi, K.; Yamashita, M.; Watashige, T.; Kasahara, S.; Matsuda, Y.; et al. Dome-Shaped Magnetic Order Competing with High-Temperature Superconductivity at High Pressures in FeSe. *Nat. Commun.* **2016**, *7*, 12146. [CrossRef]
18. Sun, J.P.; Ye, G.Z.; Shahi, P.; Yan, J.-Q.; Matsuura, K.; Kontani, H.; Zhang, G.M.; Zhou, Q.; Sales, B.C.; Shibauchi, T.; et al. High- $T_c$  Superconductivity in FeSe at High Pressure: Dominant Hole Carriers and Enhanced Spin Fluctuations. *Phys. Rev. Lett.* **2017**, *118*, 147004. [CrossRef]
19. Gati, E.; Böhmer, A.E.; Bud'ko, S.L.; Canfield, P.C. Bulk Superconductivity and Role of Fluctuations in the Iron-Based Superconductor FeSe at High Pressures. *Phys. Rev. Lett.* **2019**, *123*, 167002. [CrossRef]
20. Lu, X.F.; Wang, N.Z.; Wu, H.; Wu, Y.P.; Zhao, D.; Zeng, X.Z.; Luo, X.G.; Wu, T.; Bao, W.; Zhang, G.H.; et al. Coexistence of Superconductivity and Antiferromagnetism in  $(\text{Li}_{0.8}\text{Fe}_{0.2})\text{OHFeSe}$ . *Nat. Mater.* **2015**, *14*, 325–329. [CrossRef]
21. Shi, M.Z.; Wang, N.Z.; Lei, B.; Ying, J.J.; Zhu, C.S.; Sun, Z.L.; Cui, J.H.; Meng, F.B.; Shang, C.; Ma, L.K.; et al. FeSe-Based Superconductors with a Superconducting Transition Temperature of 50 K. *New J. Phys.* **2018**, *20*, 123007. [CrossRef]
22. Lei, B.; Cui, J.H.; Xiang, Z.J.; Shang, C.; Wang, N.Z.; Ye, G.J.; Luo, X.G.; Wu, T.; Sun, Z.; Chen, X.H. Evolution of High-Temperature Superconductivity from a Low- $T_c$  Phase Tuned by Carrier Concentration in FeSe Thin Flakes. *Phys. Rev. Lett.* **2016**, *116*, 077002. [CrossRef]
23. Meng, Y.; Xing, X.; Yi, X.; Li, B.; Zhou, N.; Li, M.; Zhang, Y.; Wei, W.; Feng, J.; Terashima, K.; et al. Protonation-Induced Discrete Superconducting Phases in Bulk FeSe Single Crystals. *Phys. Rev. B* **2022**, *105*, 134506. [CrossRef]
24. Meng, Y.; Wei, W.; Xing, X.; Yi, X.; Zhou, N.; Zhang, Y.; Liu, W.; Sun, Y.; Shi, Z. Significant Enhancement of Critical Current Density in  $\text{H}^+$ -Intercalated FeSe Single Crystal. *Supercond. Sci. Technol.* **2022**, *35*, 075012. [CrossRef]
25. Shi, X.; Han, Z.-Q.; Peng, X.-L.; Richard, P.; Qian, T.; Wu, X.-X.; Qiu, M.-W.; Wang, S.C.; Hu, J.P.; Sun, Y.-J.; et al. Enhanced Superconductivity Accompanying a Lifshitz Transition in Electron-Doped FeSe Monolayer. *Nat. Commun.* **2017**, *8*, 14988. [CrossRef] [PubMed]
26. Wen, C.H.P.; Xu, H.C.; Chen, C.; Huang, Z.C.; Lou, X.; Pu, Y.J.; Song, Q.; Xie, B.P.; Abdel-Hafiez, M.; Chareev, D.A.; et al. Anomalous Correlation Effects and Unique Phase Diagram of Electron-Doped FeSe Revealed by Photoemission Spectroscopy. *Nat. Commun.* **2016**, *7*, 10840. [CrossRef] [PubMed]
27. Ge, J.-F.; Liu, Z.-L.; Liu, C.; Gao, C.-L.; Qian, D.; Xue, Q.-K.; Liu, Y.; Jia, J.-F. Superconductivity above 100 K in Single-Layer FeSe Films on Doped  $\text{SrTiO}_3$ . *Nat. Mater.* **2015**, *14*, 285–289. [CrossRef] [PubMed]
28. Qing-Yan, W.; Zhi, L.; Wen-Hao, Z.; Zuo-Cheng, Z.; Jin-Song, Z.; Wei, L.; Hao, D.; Yun-Bo, O.; Peng, D.; Kai, C.; et al. Interface-Induced High-Temperature Superconductivity in Single Unit-Cell FeSe Films on  $\text{SrTiO}_3$ . *Chin. Phys. Lett.* **2012**, *29*, 037402.
29. Reiss, P.; Watson, M.D.; Kim, T.K.; Haghaghirad, A.A.; Woodruff, D.N.; Bruma, M.; Clarke, S.J.; Coldea, A.I. Suppression of Electronic Correlations by Chemical Pressure from FeSe to FeS. *Phys. Rev. B* **2017**, *96*, 121103. [CrossRef]
30. Sato, Y.; Kasahara, S.; Taniguchi, T.; Xing, X.; Kasahara, Y.; Tokiwa, Y.; Yamakawa, Y.; Kontani, H.; Shibauchi, T.; Matsuda, Y. Abrupt Change of the Superconducting Gap Structure at the Nematic Critical Point in  $\text{FeSe}_{1-x}\text{S}_x$ . *Proc. Natl. Acad. Sci. USA* **2018**, *115*, 1227–1231. [CrossRef]
31. Wiecki, P.; Rana, K.; Böhmer, A.E.; Lee, Y.; Bud'ko, S.L.; Canfield, P.C.; Furukawa, Y. Persistent Correlation between Superconductivity and Antiferromagnetic Fluctuations near a Nematic Quantum Critical Point in  $\text{FeSe}_{1-x}\text{S}_x$ . *Phys. Rev. B* **2018**, *98*, 020507. [CrossRef]
32. Licciardello, S.; Buhot, J.; Lu, J.; Ayres, J.; Kasahara, S.; Matsuda, Y.; Shibauchi, T.; Hussey, N.E. Electrical Resistivity across a Nematic Quantum Critical Point. *Nature* **2019**, *567*, 213–217. [CrossRef]
33. Yi, X.; Xing, X.; Qin, L.; Feng, J.; Li, M.; Zhang, Y.; Meng, Y.; Zhou, N.; Sun, Y.; Shi, Z. Hydrothermal Synthesis and Complete Phase Diagram of  $\text{FeSe}_{1-x}\text{S}_x$  ( $0 \leq x \leq 1$ ) Single Crystals. *Phys. Rev. B* **2021**, *103*, 144501. [CrossRef]
34. Lai, X.; Zhang, H.; Wang, Y.; Wang, X.; Zhang, X.; Lin, J.; Huang, F. Observation of Superconductivity in Tetragonal FeS. *J. Am. Chem. Soc.* **2015**, *137*, 10148–10151. [CrossRef]
35. Matsuura, K.; Mizukami, Y.; Arai, Y.; Sugimura, Y.; Maejima, N.; Machida, A.; Watanuki, T.; Fukuda, T.; Yajima, T.; Hiroi, Z.; et al. Maximizing  $T_c$  by Tuning Nematicity and Magnetism in  $\text{FeSe}_{1-x}\text{S}_x$  Superconductors. *Nat. Commun.* **2017**, *8*, 1143. [CrossRef]

36. Terao, K.; Kashiwagi, T.; Shizu, T.; Klemm, R.A.; Kadokawa, K. Superconducting and Tetragonal-to-Orthorhombic Transitions in Single Crystals of  $\text{FeSe}_{1-x}\text{Te}_x$  ( $0 \leq x \leq 0.61$ ). *Phys. Rev. B* **2019**, *100*, 224516. [CrossRef]
37. Mukasa, K.; Matsuura, K.; Qiu, M.; Saito, M.; Sugimura, Y.; Ishida, K.; Otani, M.; Onishi, Y.; Mizukami, Y.; Hashimoto, K.; et al. High-Pressure Phase Diagrams of  $\text{FeSe}_{1-x}\text{Te}_x$ : Correlation between Suppressed Nematicity and Enhanced Superconductivity. *Nat. Commun.* **2021**, *12*, 381. [CrossRef]
38. Xing, X.; Sun, Y.; Yi, X.; Li, M.; Feng, J.; Meng, Y.; Zhang, Y.; Li, W.; Zhou, N.; He, X.; et al. Electronic Transport Properties and Hydrostatic Pressure Effect of  $\text{FeSe}_{0.67}\text{Te}_{0.33}$  Single Crystals Free of Phase Separation. *Supercond. Sci. Technol.* **2021**, *34*, 055006. [CrossRef]
39. Sun, Y.; Yamada, T.; Pyon, S.; Tamegai, T. Influence of Interstitial Fe to the Phase Diagram of  $\text{Fe}_{1+y}\text{Te}_{1-x}\text{Se}_x$  Single Crystals. *Sci. Rep.* **2016**, *6*, 32290. [CrossRef]
40. Liu, T.J.; Hu, J.; Qian, B.; Fobes, D.; Mao, Z.Q.; Bao, W.; Reehuis, M.; Kimber, S.A.J.; Prokeš, K.; Matas, S.; et al. From  $(\pi, 0)$  Magnetic Order to Superconductivity with  $(\pi, \pi)$  Magnetic Resonance in  $\text{Fe}_{1.02}\text{Te}_{1-x}\text{Se}_x$ . *Nat. Mater.* **2010**, *9*, 718–720. [CrossRef] [PubMed]
41. Sun, Y.; Shi, Z.; Tamegai, T. Review of Annealing Effects and Superconductivity in  $\text{Fe}_{1+y}\text{Te}_{1-x}\text{Se}_x$  Superconductors. *Supercond. Sci. Technol.* **2019**, *32*, 103001. [CrossRef]
42. Chen, D.P.; Lin, C.T. The Growth of 122 and 11 Iron-Based Superconductor Single Crystals and the Influence of Doping. *Supercond. Sci. Technol.* **2014**, *27*, 103002. [CrossRef]
43. Bao, W.; Qiu, Y.; Huang, Q.; Green, M.A.; Zajdel, P.; Fitzsimmons, M.R.; Zhernenkov, M.; Chang, S.; Fang, M.; Qian, B.; et al. Tunable  $(\Delta\pi, \Delta\pi)$ -Type Antiferromagnetic Order in  $\alpha$ -Fe(Se,Te) Superconductors. *Phys. Rev. Lett.* **2009**, *102*, 247001. [CrossRef] [PubMed]
44. Li, S.; de la Cruz, C.; Huang, Q.; Chen, Y.; Lynn, J.W.; Hu, J.; Huang, Y.-L.; Hsu, F.-C.; Yeh, K.-W.; Wu, M.-K.; et al. First-Order Magnetic and Structural Phase Transitions in  $\text{Fe}_{1+y}\text{Se}_x\text{Te}_{1-x}$ . *Phys. Rev. B* **2009**, *79*, 054503. [CrossRef]
45. Lee, P.A.; Nagaosa, N.; Wen, X.-G. Doping a Mott Insulator: Physics of High-Temperature Superconductivity. *Rev. Mod. Phys.* **2006**, *78*, 17–85. [CrossRef]
46. Liu, Z.K.; He, R.-H.; Lu, D.H.; Yi, M.; Chen, Y.L.; Hashimoto, M.; Moore, R.G.; Mo, S.-K.; Nowadnick, E.A.; Hu, J.; et al. Measurement of Coherent Polarons in the Strongly Coupled Antiferromagnetically Ordered Iron-Chalcogenide  $\text{Fe}_{1.02}\text{Te}$  Using Angle-Resolved Photoemission Spectroscopy. *Phys. Rev. Lett.* **2013**, *110*, 037003. [CrossRef]
47. Fobes, D.; Zaliznyak, I.A.; Xu, Z.; Zhong, R.; Gu, G.; Tranquada, J.M.; Harriger, L.; Singh, D.; Garlea, V.O.; Lumsden, M.; et al. Ferro-Orbital Ordering Transition in Iron Telluride  $\text{Fe}_{1+y}\text{Te}$ . *Phys. Rev. Lett.* **2014**, *112*, 187202. [CrossRef]
48. Mizuguchi, Y.; Tomioka, F.; Tsuda, S.; Yamaguchi, T.; Takano, Y. Substitution Effects on FeSe Superconductor. *J. Phys. Soc. Jpn.* **2009**, *78*, 074712. [CrossRef]
49. McQueen, T.M.; Huang, Q.; Ksenofontov, V.; Felser, C.; Xu, Q.; Zandbergen, H.; Hor, Y.S.; Allred, J.; Williams, A.J.; Qu, D.; et al. Extreme Sensitivity of Superconductivity to Stoichiometry in  $\text{Fe}_{1+\delta}\text{Se}$ . *Phys. Rev. B* **2009**, *79*, 014522. [CrossRef]
50. Wen, J.; Xu, G.; Gu, G.; Tranquada, J.M.; Birgeneau, R.J. Interplay between Magnetism and Superconductivity in Iron-Chalcogenide Superconductors: Crystal Growth and Characterizations. *Rep. Prog. Phys.* **2011**, *74*, 124503. [CrossRef]
51. Fang, M.H.; Pham, H.M.; Qian, B.; Liu, T.J.; Vehstedt, E.K.; Liu, Y.; Spinu, L.; Mao, Z.Q. Superconductivity Close to Magnetic Instability in  $\text{Fe}(\text{Se}_{1-x}\text{Te}_x)_{0.82}$ . *Phys. Rev. B* **2008**, *78*, 224503. [CrossRef]
52. Mizuguchi, Y.; Takano, Y. Review of Fe Chalcogenides as the Simplest Fe-Based Superconductor. *J. Phys. Soc. Jpn.* **2010**, *79*, 102001. [CrossRef]
53. Liu, T.J.; Ke, X.; Qian, B.; Hu, J.; Fobes, D.; Vehstedt, E.K.; Pham, H.; Yang, J.H.; Fang, M.H.; Spinu, L.; et al. Charge-Carrier Localization Induced by Excess Fe in the Superconductor  $\text{Fe}_{1+y}\text{Te}_{1-x}\text{Se}_x$ . *Phys. Rev. B* **2009**, *80*, 174509. [CrossRef]
54. Ieki, E.; Nakayama, K.; Miyata, Y.; Sato, T.; Miao, H.; Xu, N.; Wang, X.-P.; Zhang, P.; Qian, T.; Richard, P.; et al. Evolution from Incoherent to Coherent Electronic States and Its Implications for Superconductivity in  $\text{FeTe}_{1-x}\text{Se}_x$ . *Phys. Rev. B* **2014**, *89*, 140506. [CrossRef]
55. Sun, Y.; Taen, T.; Yamada, T.; Pyon, S.; Nishizaki, T.; Shi, Z.; Tamegai, T. Multiband Effects and Possible Dirac Fermions in  $\text{Fe}_{1+y}\text{Te}_{0.6}\text{Se}_{0.4}$ . *Phys. Rev. B* **2014**, *89*, 144512. [CrossRef]
56. Katayama, N.; Ji, S.; Louca, D.; Lee, S.; Fujita, M.; Sato, T.J.; Wen, J.; Xu, Z.; Gu, G.; Xu, G.; et al. Investigation of the Spin-Glass Regime between the Antiferromagnetic and Superconducting Phases in  $\text{Fe}_{1+y}\text{Se}_x\text{Te}_{1-x}$ . *J. Phys. Soc. Jpn.* **2010**, *79*, 113702. [CrossRef]
57. Otsuka, T.; Hagiwara, S.; Koshika, Y.; Adachi, S.; Usui, T.; Sasaki, N.; Sasaki, S.; Yamaguchi, S.; Nakanishi, Y.; Yoshizawa, M.; et al. Incoherent-Coherent Crossover and the Pseudogap in Te-Annealed Superconducting  $\text{Fe}_{1+y}\text{Te}_{1-x}\text{Se}_x$  Revealed by Magnetotransport Measurements. *Phys. Rev. B* **2019**, *99*, 184505. [CrossRef]
58. Maletz, J.; Zabolotnyy, V.B.; Evtushinsky, D.V.; Thirupathaiah, S.; Wolter, A.U.B.; Harnagea, L.; Yaresko, A.N.; Vasiliev, A.N.; Chareev, D.A.; Böhmer, A.E.; et al. Unusual Band Renormalization in the Simplest Iron-Based Superconductor  $\text{FeSe}_{1-x}$ . *Phys. Rev. B* **2014**, *89*, 220506. [CrossRef]
59. Kasahara, S.; Watashige, T.; Hanaguri, T.; Kohsaka, Y.; Yamashita, T.; Shimoyama, Y.; Mizukami, Y.; Endo, R.; Ikeda, H.; Aoyama, K.; et al. Field-Induced Superconducting Phase of FeSe in the BCS-BEC Cross-Over. *Proc. Natl. Acad. Sci. USA* **2014**, *111*, 16309–16313. [CrossRef]
60. Watson, M.D.; Kim, T.K.; Haghaghirad, A.A.; Davies, N.R.; McCollam, A.; Narayanan, A.; Blake, S.F.; Chen, Y.L.; Ghannadzadeh, S.; Schofield, A.J.; et al. Emergence of the Nematic Electronic State in FeSe. *Phys. Rev. B* **2015**, *91*, 155106. [CrossRef]

61. Zhang, S.B.; Sun, Y.P.; Zhu, X.D.; Zhu, X.B.; Wang, B.S.; Li, G.; Lei, H.C.; Luo, X.; Yang, Z.R.; Song, W.H.; et al. Crystal Growth and Superconductivity of  $\text{FeSe}_x$ . *Supercond. Sci. Technol.* **2008**, *22*, 015020. [[CrossRef](#)]
62. Mok, B.H.; Rao, S.M.; Ling, M.C.; Wang, K.J.; Ke, C.T.; Wu, P.M.; Chen, C.L.; Hsu, F.C.; Huang, T.W.; Luo, J.Y.; et al. Growth and Investigation of Crystals of the New Superconductor  $\alpha$ -FeSe from KCl Solutions. *Cryst. Growth Des.* **2009**, *9*, 3260–3264. [[CrossRef](#)]
63. Patel, U.; Hua, J.; Yu, S.H.; Avci, S.; Xiao, Z.L.; Claus, H.; Schlueter, J.; Vlasko-Vlasov, V.V.; Welp, U.; Kwok, W.K. Growth and Superconductivity of  $\text{FeSe}_x$  Crystals. *Appl. Phys. Lett.* **2009**, *94*, 082508. [[CrossRef](#)]
64. Tissen, V.G.; Ponyatovsky, E.G.; Nefedova, M.V.; Titov, A.N.; Fedorenko, V.V. Effects of Pressure-Induced Phase Transitions on Superconductivity in Single-Crystal  $\text{Fe}_{1.02}\text{Se}$ . *Phys. Rev. B* **2009**, *80*, 092507. [[CrossRef](#)]
65. Wu, M.K.; Hsu, F.C.; Yeh, K.W.; Huang, T.W.; Luo, J.Y.; Wang, M.J.; Chang, H.H.; Chen, T.K.; Rao, S.M.; Mok, B.H.; et al. The Development of the Superconducting  $\text{PbO}$ -Type  $\beta$ -FeSe and Related Compounds. *Phys. C Supercond.* **2009**, *469*, 340–349. [[CrossRef](#)]
66. Malavasi, L.; Margadonna, S. Structure–Properties Correlations in Fe Chalcogenide Superconductors. *Chem. Soc. Rev.* **2012**, *41*, 3897–3911. [[CrossRef](#)]
67. Hu, R.; Lei, H.; Abeykoon, M.; Bozin, E.S.; Billinge, S.J.L.; Warren, J.B.; Siegrist, T.; Petrovic, C. Synthesis, Crystal Structure, and Magnetism of  $\beta\text{-Fe}_{1.00(2)}\text{Se}_{1.00(3)}$  Single Crystals. *Phys. Rev. B* **2011**, *83*, 224502. [[CrossRef](#)]
68. Chareev, D.; Osadchii, E.; Kuzmicheva, T.; Lin, J.-Y.; Kuzmichev, S.; Volkova, O.; Vasiliev, A. Single Crystal Growth and Characterization of Tetragonal  $\text{FeSe}_{1-x}$  Superconductors. *CrystEngComm* **2013**, *15*, 1989–1993. [[CrossRef](#)]
69. Wu, M.K.; Wu, P.M.; Wen, Y.C.; Wang, M.J.; Lin, P.H.; Lee, W.C.; Chen, T.K.; Chang, C.C. An Overview of the Fe-Chalcogenide Superconductors. *J. Phys. D Appl. Phys.* **2015**, *48*, 323001. [[CrossRef](#)]
70. Yu, R.; Zhu, J.-X.; Si, Q. Orbital Selectivity Enhanced by Nematic Order in FeSe. *Phys. Rev. Lett.* **2018**, *121*, 227003. [[CrossRef](#)]
71. Massat, P.; Farina, D.; Paul, I.; Karlsson, S.; Strobel, P.; Toulemonde, P.; Méasson, M.-A.; Cazayous, M.; Sacuto, A.; Kasahara, S.; et al. Charge-Induced Nematicity in FeSe. *Proc. Natl. Acad. Sci. USA* **2016**, *113*, 9177–9181. [[CrossRef](#)]
72. Farrar, L.S.; Zajicek, Z.; Morfoot, A.B.; Bristow, M.; Humphries, O.S.; Haghimirad, A.A.; McCollam, A.; Bending, S.J.; Coldea, A.I. Unconventional Localization of Electrons inside of a Nematic Electronic Phase. *Proc. Natl. Acad. Sci. USA* **2022**, *119*, e2200405119. [[CrossRef](#)] [[PubMed](#)]
73. Sun, Y.; Pyon, S.; Tamegai, T.; Kobayashi, R.; Watashige, T.; Kasahara, S.; Matsuda, Y.; Shibauchi, T. Critical Current Density, Vortex Dynamics, and Phase Diagram of Single-Crystal FeSe. *Phys. Rev. B* **2015**, *92*, 144509. [[CrossRef](#)]
74. Okamoto, H. The Fe–Se (Iron–Selenium) System. *JPE* **1991**, *12*, 383–389. [[CrossRef](#)]
75. Böhmer, A.E.; Taufour, V.; Straszheim, W.E.; Wolf, T.; Canfield, P.C. Variation of Transition Temperatures and Residual Resistivity Ratio in Vapor-Grown FeSe. *Phys. Rev. B* **2016**, *94*, 024526. [[CrossRef](#)]
76. Hosoi, S.; Matsuura, K.; Ishida, K.; Wang, H.; Mizukami, Y.; Watashige, T.; Kasahara, S.; Matsuda, Y.; Shibauchi, T. Nematic Quantum Critical Point without Magnetism in  $\text{FeSe}_{1-x}\text{S}_x$  Superconductors. *Proc. Natl. Acad. Sci. USA* **2016**, *113*, 8139–8143. [[CrossRef](#)]
77. Bristow, M.; Reiss, P.; Haghimirad, A.A.; Zajicek, Z.; Singh, S.J.; Wolf, T.; Graf, D.; Knafo, W.; McCollam, A.; Coldea, A.I. Anomalous High-Magnetic Field Electronic State of the Nematic Superconductors  $\text{FeSe}_{1-x}\text{S}_x$ . *Phys. Rev. Res.* **2020**, *2*, 013309. [[CrossRef](#)]
78. Coldea, A.I. Electronic Nematic States Tuned by Isoelectronic Substitution in Bulk  $\text{FeSe}_{1-x}\text{S}_x$ . *Front. Phys.* **2021**, *8*, 594500. [[CrossRef](#)]
79. Watson, M.D.; Kim, T.K.; Haghimirad, A.A.; Blake, S.F.; Davies, N.R.; Hoesch, M.; Wolf, T.; Coldea, A.I. Suppression of Orbital Ordering by Chemical Pressure in  $\text{FeSe}_{1-x}\text{S}_x$ . *Phys. Rev. B* **2015**, *92*, 121108. [[CrossRef](#)]
80. Sun, Y.; Pyon, S.; Tamegai, T. Electron Carriers with Possible Dirac-Cone-like Dispersion in  $\text{FeSe}_{1-x}\text{S}_x$  ( $x = 0$  and 0.14) Single Crystals Triggered by Structural Transition. *Phys. Rev. B* **2016**, *93*, 104502. [[CrossRef](#)]
81. Licciardello, S.; Maksimovic, N.; Ayres, J.; Buhot, J.; Čulo, M.; Bryant, B.; Kasahara, S.; Matsuda, Y.; Shibauchi, T.; Nagarajan, V.; et al. Coexistence of Orbital and Quantum Critical Magnetoresistance in  $\text{FeSe}_{1-x}\text{S}_x$ . *Phys. Rev. Res.* **2019**, *1*, 023011. [[CrossRef](#)]
82. Lin, H.; Li, Y.; Deng, Q.; Xing, J.; Liu, J.; Zhu, X.; Yang, H.; Wen, H.-H. Multiband Superconductivity and Large Anisotropy in FeS Crystals. *Phys. Rev. B* **2016**, *93*, 144505. [[CrossRef](#)]
83. Ying, T.P.; Lai, X.F.; Hong, X.C.; Xu, Y.; He, L.P.; Zhang, J.; Wang, M.X.; Yu, Y.J.; Huang, F.Q.; Li, S.Y. Nodal Superconductivity in FeS: Evidence from Quasiparticle Heat Transport. *Phys. Rev. B* **2016**, *94*, 100504. [[CrossRef](#)]
84. Borg, C.K.H.; Zhou, X.; Eckberg, C.; Campbell, D.J.; Saha, S.R.; Paglione, J.; Rodriguez, E.E. Strong Anisotropy in Nearly Ideal Tetrahedral Superconducting FeS Single Crystals. *Phys. Rev. B* **2016**, *93*, 094522. [[CrossRef](#)]
85. Guo, Z.; Sun, F.; Chen, Y.; Mao, Y.; Wan, L.; Yan, X.; Yang, Y.; Yuan, W. Synthesis, Structure and Superconductivity of  $\text{FeSe}_{1-x}\text{S}_x$  ( $0 \leq x \leq 1$ ) Solid Solution Crystals. *CrystEngComm* **2019**, *21*, 2994–2999. [[CrossRef](#)]
86. Yuan, D.; Huang, Y.; Ni, S.; Zhou, H.; Mao, Y.; Hu, W.; Yuan, J.; Jin, K.; Zhang, G.; Dong, X.; et al. Synthesis of Large FeSe Superconductor Crystals via Ion Release/Introduction and Property Characterization\*. *Chin. Phys. B* **2016**, *25*, 077404. [[CrossRef](#)]
87. Liu, Y.; Wang, A.; Ivanovski, V.N.; Du, Q.; Koteski, V.; Petrovic, C. Thermoelectricity and Electronic Correlation Enhancement in FeS by Light Se Doping. *Phys. Rev. B* **2022**, *105*, 045133. [[CrossRef](#)]
88. Pachmayr, U.; Fehn, N.; Johrendt, D. Structural Transition and Superconductivity in Hydrothermally Synthesized FeX (X = S, Se). *Chem. Commun.* **2015**, *52*, 194–197. [[CrossRef](#)]

89. Ishida, K.; Onishi, Y.; Tsujii, M.; Mukasa, K.; Qiu, M.; Saito, M.; Sugimura, Y.; Matsuura, K.; Mizukami, Y.; Hashimoto, K.; et al. Pure Nematic Quantum Critical Point Accompanied by a Superconducting Dome. *Proc. Natl. Acad. Sci. USA* **2022**, *119*, e2110501119. [[CrossRef](#)]
90. Wang, D.; Kong, L.; Fan, P.; Chen, H.; Zhu, S.; Liu, W.; Cao, L.; Sun, Y.; Du, S.; Schneeloch, J.; et al. Evidence for Majorana Bound States in an Iron-Based Superconductor. *Science* **2018**, *362*, 333–335. [[CrossRef](#)]
91. Zhang, P.; Yaji, K.; Hashimoto, T.; Ota, Y.; Kondo, T.; Okazaki, K.; Wang, Z.; Wen, J.; Gu, G.D.; Ding, H.; et al. Observation of Topological Superconductivity on the Surface of an Iron-Based Superconductor. *Science* **2018**, *360*, 182–186. [[CrossRef](#)] [[PubMed](#)]
92. Si, W.; Han, S.J.; Shi, X.; Ehrlich, S.N.; Jaroszynski, J.; Goyal, A.; Li, Q. High Current Superconductivity in  $\text{FeSe}_{0.5}\text{Te}_{0.5}$ -Coated Conductors at 30 Tesla. *Nat. Commun.* **2013**, *4*, 1347. [[CrossRef](#)] [[PubMed](#)]
93. Noji, T.; Suzuki, T.; Abe, H.; Adachi, T.; Kato, M.; Koike, Y. Growth, Annealing Effects on Superconducting and Magnetic Properties, and Anisotropy of  $\text{FeSe}_{1-x}\text{Te}_x$  ( $0.5 \leq x \leq 1$ ) Single Crystals. *J. Phys. Soc. Jpn.* **2010**, *79*, 084711. [[CrossRef](#)]
94. Okazaki, K.; Ito, Y.; Ota, Y.; Kotani, Y.; Shimojima, T.; Kiss, T.; Watanabe, S.; Chen, C.-T.; Niitaka, S.; Hanaguri, T.; et al. Evidence for a  $\text{Cos}(4\phi)$  Modulation of the Superconducting Energy Gap of Optimally Doped  $\text{FeTe}_{0.6}\text{Se}_{0.4}$  Single Crystals Using Laser Angle-Resolved Photoemission Spectroscopy. *Phys. Rev. Lett.* **2012**, *109*, 237011. [[CrossRef](#)]
95. Sales, B.C.; Sefat, A.S.; McGuire, M.A.; Jin, R.Y.; Mandrus, D.; Mozharivskyj, Y. Bulk Superconductivity at 14 K in Single Crystals of  $\text{Fe}_{1+y}\text{Te}_x\text{Se}_{1-x}$ . *Phys. Rev. B* **2009**, *79*, 094521. [[CrossRef](#)]
96. Yeh, K.W.; Ke, C.T.; Huang, T.W.; Chen, T.K.; Huang, Y.L.; Wu, P.M.; Wu, M.K. Superconducting  $\text{FeSe}_{1-x}\text{Te}_x$  Single Crystals Grown by Optical Zone-Melting Technique. *Cryst. Growth Des.* **2009**, *9*, 4847–4851. [[CrossRef](#)]
97. Sun, Y.; Taen, T.; Yamada, T.; Tsuchiya, Y.; Pyon, S.; Tamegai, T. Evolution of Superconducting and Transport Properties in Annealed  $\text{FeTe}_{1-x}\text{Se}_x$  ( $0.1 \leq x \leq 0.4$ ) Multiband Superconductors. *Supercond. Sci. Technol.* **2015**, *28*, 044002. [[CrossRef](#)]
98. Fujitsu, S.; Matsuishi, S.; Hosono, H. Iron Based Superconductors Processing and Properties. *Int. Mater. Rev.* **2012**, *57*, 311–327. [[CrossRef](#)]
99. Taen, T.; Tsuchiya, Y.; Nakajima, Y.; Tamegai, T. Superconductivity at  $T_c \sim 14$  K in Single-Crystalline  $\text{FeTe}_{0.61}\text{Se}_{0.39}$ . *Phys. Rev. B* **2009**, *80*, 092502. [[CrossRef](#)]
100. Komiya, S.; Hanawa, M.; Tsukada, I.; Maeda, A. Effect of Vacuum Annealing on Superconductivity in Fe(Se,Te) Single Crystals. *J. Phys. Soc. Jpn.* **2013**, *82*, 064710. [[CrossRef](#)]
101. Hu, J.; Wang, G.C.; Qian, B.; Mao, Z.Q. Inhomogeneous Superconductivity Induced by Interstitial Fe Deintercalation in Oxidizing-Agent-Annealed and  $\text{HNO}_3$ -Treated  $\text{Fe}_{1+y}(\text{Te}_{1-x}\text{Se}_x)$ . *Supercond. Sci. Technol.* **2012**, *25*, 084011. [[CrossRef](#)]
102. Sun, Y.; Tsuchiya, Y.; Taen, T.; Yamada, T.; Pyon, S.; Sugimoto, A.; Ekino, T.; Shi, Z.; Tamegai, T. Dynamics and Mechanism of Oxygen Annealing in  $\text{Fe}_{1+y}\text{Te}_{0.6}\text{Se}_{0.4}$  Single Crystal. *Sci. Rep.* **2014**, *4*, 4585. [[CrossRef](#)]
103. Rodriguez, E.E.; Stock, C.; Hsieh, P.-Y.; Butch, N.P.; Paglione, J.; Green, M.A. Chemical Control of Interstitial Iron Leading to Superconductivity in  $\text{Fe}_{1+x}\text{Te}_{0.7}\text{Se}_{0.3}$ . *Chem. Sci.* **2011**, *2*, 1782–1787. [[CrossRef](#)]
104. Koshika, Y.; Usui, T.; Adachi, S.; Watanabe, T.; Sakano, K.; Simayi, S.; Yoshizawa, M. Effects of Annealing under Tellurium Vapor for  $\text{Fe}_{1.03}\text{Te}_{0.8}\text{Se}_{0.2}$  Single Crystals. *J. Phys. Soc. Jpn.* **2013**, *82*, 023703. [[CrossRef](#)]
105. Sun, Y.; Tsuchiya, Y.; Yamada, T.; Taen, T.; Pyon, S.; Shi, Z.; Tamegai, T. Bulk Superconductivity in  $\text{Fe}_{1+y}\text{Te}_{1-x}\text{Se}_x$  Induced by Annealing in Se and S Vapor. *J. Phys. Soc. Jpn.* **2013**, *82*, 115002. [[CrossRef](#)]
106. Zhou, W.; Sun, Y.; Zhang, S.; Zhuang, J.; Yuan, F.; Li, X.; Shi, Z.; Yamada, T.; Tsuchiya, Y.; Tamegai, T. Bulk Superconductivity in  $\text{Fe}_{1+y}\text{Te}_{0.6}\text{Se}_{0.4}$  Induced by Removal of Excess Fe. *J. Phys. Soc. Jpn.* **2014**, *83*, 064704. [[CrossRef](#)]
107. Yamada, T.; Sun, Y.; Pyon, S.; Tamegai, T. Effects of Pnictogen Atmosphere Annealing on  $\text{Fe}_{1+y}\text{Te}_{0.6}\text{Se}_{0.4}$ . *J. Phys. Soc. Jpn.* **2016**, *85*, 024712. [[CrossRef](#)]
108. Chen, J.; Sun, Y.; Yamada, T.; Pyon, S.; Tamegai, T. Effects of Iodine Annealing on  $\text{Fe}_{1+y}\text{Te}_{0.6}\text{Se}_{0.4}$ . *J. Phys. Soc. Jpn.* **2016**, *85*, 104714. [[CrossRef](#)]
109. Ge, J.; Cao, S.; Shen, S.; Yuan, S.; Kang, B.; Zhang, J. Superconducting Properties of Highly Oriented  $\text{Fe}_{1.03}\text{Te}_{0.55}\text{Se}_{0.45}$  with Excess Fe. *Solid State Commun.* **2010**, *150*, 1641–1645. [[CrossRef](#)]
110. Mizuguchi, Y.; Tomioka, F.; Tsuda, S.; Yamaguchi, T.; Takano, Y. Superconductivity in S-Substituted FeTe. *Appl. Phys. Lett.* **2009**, *94*, 012503. [[CrossRef](#)]
111. Hu, R.; Bozin, E.S.; Warren, J.B.; Petrovic, C. Superconductivity, Magnetism, and Stoichiometry of Single Crystals of  $\text{Fe}_{1+y}(\text{Te}_{1-x}\text{S}_x)_z$ . *Phys. Rev. B* **2009**, *80*, 214514. [[CrossRef](#)]
112. Lei, H.; Hu, R.; Choi, E.S.; Warren, J.B.; Petrovic, C. Effects of Excess Fe on Upper Critical Field and Magnetotransport in  $\text{Fe}_{1+y}(\text{Te}_{1-x}\text{S}_x)_z$ . *Phys. Rev. B* **2010**, *81*, 184522. [[CrossRef](#)]
113. Lei, H.; Hu, R.; Choi, E.S.; Petrovic, C. Thermally Activated Energy and Flux-Flow Hall Effect of  $\text{Fe}_{1+y}(\text{Te}_{1-x}\text{S}_x)_z$ . *Phys. Rev. B* **2010**, *82*, 134525. [[CrossRef](#)]
114. Mizuguchi, Y.; Deguchi, K.; Tsuda, S.; Yamaguchi, T.; Takano, Y. Moisture-Induced Superconductivity in  $\text{FeTe}_{0.8}\text{S}_{0.2}$ . *Phys. Rev. B* **2010**, *81*, 214510. [[CrossRef](#)]
115. Wang, A.; Kampert, E.; Saadaoui, H.; Luetkens, H.; Hu, R.; Morenzoni, E.; Wosnitza, J.; Petrovic, C. Normal State above the Upper Critical Field in  $\text{Fe}_{1+y}\text{Te}_{1-x}(\text{Se}, \text{S})_x$ . *Phys. Rev. B* **2017**, *95*, 184504. [[CrossRef](#)]
116. Mizuguchi, Y.; Deguchi, K.; Kawasaki, Y.; Ozaki, T.; Nagao, M.; Tsuda, S.; Yamaguchi, T.; Takano, Y. Superconductivity in Oxygen-Annealed  $\text{FeTe}_{1-x}\text{S}_x$  Single Crystal. *J. Appl. Phys.* **2011**, *109*, 013914. [[CrossRef](#)]

117. Zhang, Z.T.; Yang, Z.R.; Li, L.; Pi, L.; Tan, S.; Zhang, Y.H. Annealing Effects on Superconductivity and Magnetism in  $\text{Fe}_{1+y}\text{Te}_{1-x}\text{S}_x$  Single Crystals. *J. Appl. Phys.* **2012**, *111*, 07E118. [[CrossRef](#)]
118. Awana, V.P.S.; Pal, A.; Vajpayee, A.; Gahtori, B.; Kishan, H. Superconductivity and Thermal Properties of Sulphur Doped FeTe with Effect of Oxygen Post Annealing. *Phys. C Supercond.* **2011**, *471*, 77–82. [[CrossRef](#)]
119. Dong, C.; Wang, H.; Mao, Q.; Khan, R.; Zhou, X.; Li, C.; Yang, J.; Chen, B.; Fang, M. Phase Diagram and Annealing Effect for  $\text{Fe}_{1+\delta}\text{Te}_{1-x}\text{S}_x$  Single Crystals. *J. Phys. Condens. Matter* **2013**, *25*, 385701. [[CrossRef](#)]
120. Yamazaki, T.; Sakurai, T.; Yaguchi, H. Size Dependence of Oxygen-Annealing Effects on Superconductivity of  $\text{Fe}_{1+y}\text{Te}_{1-x}\text{S}_x$ . *J. Phys. Soc. Jpn.* **2016**, *85*, 114712. [[CrossRef](#)]
121. Yamamoto, K.; Yamazaki, T.; Yamanaka, T.; Ueta, D.; Yoshizawa, H.; Yaguchi, H. Anisotropic Pressure Effects on Superconductivity in  $\text{Fe}_{1+y}\text{Te}_{1-x}\text{S}_x$ . *J. Phys. Soc. Jpn.* **2018**, *87*, 054705. [[CrossRef](#)]
122. Dong, C.; Wang, H.; Yang, J.; Qian, B.; Chen, J.; Li, Z.; Yuan, H.; Fang, M. Effect of Annealing on Superconductivity in  $\text{Fe}_{1+y}(\text{Te}_{1-x}\text{S}_x)$  System. *Sci. China Phys. Mech. Astron.* **2010**, *53*, 1216–1220. [[CrossRef](#)]
123. Zhao, C.; Yi, X.; Hou, Q.; Feng, J.; Zhang, Y.; Xu, M.; Shi, Z. Hydrothermal Synthesis and Transport Properties of  $\text{FeS}_{1-x}\text{Te}_x$  ( $0 \leq x \leq 0.15$ ) Single Crystals. *J. Supercond. Nov. Magn.* **2021**, *34*, 2565–2572. [[CrossRef](#)]

**Disclaimer/Publisher's Note:** The statements, opinions and data contained in all publications are solely those of the individual author(s) and contributor(s) and not of MDPI and/or the editor(s). MDPI and/or the editor(s) disclaim responsibility for any injury to people or property resulting from any ideas, methods, instructions or products referred to in the content.